Catena 203 (2021) 105324

Contents lists available at ScienceDirect

Catena

journal homepage: www.elsevier.com/locate/catena

Pedogenic clay formation from allochthonous parent materials in a periglacial alpine critical zone

Jeffrey S. Munroe *, Peter C. Ryan, Atticus Proctor

Geology Department, Middlebury College, Middlebury, VT 05753, USA

ARTICLE INFO

Keywords:
Alpine soil
Clay minerals
Smectite
Illite
Volcanic ash
Eolian dust

ABSTRACT

This project investigated the origin of clay minerals in regolith present above quartzite bedrock in the alpine zone of the Uinta Mountains, Utah, USA. Geochemical and mineralogical analysis indicates that these clays formed through chemical weathering of two allochthonous parent materials. Smectite-rich clays, with Mg abundance distinctly higher than modern dust or local bedrock, formed through weathering of andesitic ash layers that were deposited during the Oligocene from eruptive centers in the Basin and Range. In contrast, various stages of interstratified kaolinite-illite–smectite clays have formed through weathering of mica and feldspar delivered by eolian processes that continue today. Local bedrock appears to have played only a minor role as a parent material for clay neoformation. These results demonstrate that pedogenic clay can be common even in cold climate soils and regolith overlying weathering resistant bedrock. They also emphasize that the clay inventory in soil and regolith can reflect processes that operated before modern climatic conditions were established, and reinforce the key role played by exogenous mineral inputs in the functioning of the alpine critical zone.

1. Introduction

Periglacial environments are typically considered settings in which physical weathering dominates over chemical weathering (Hall et al., 2002). This assumption is based upon the logic that rates of chemical weathering are reduced under low mean annual temperatures and diminished availability of liquid water, whereas physical weathering is enhanced by more frequent freezing and thawing (Egli et al., 2011; Hall, 1995). Studies have challenged this paradigm, however, by illuminating the degree to which chemical weathering is significant in some periglacial environments, often leading to the neoformation of clay minerals (Dixon and Thorn, 2005). For example, considerable work in the Kärkevagge region of Arctic Sweden has demonstrated that chemical weathering, including the development of interstratified clays, is widespread, particularly where pyrite-rich bedrock aids in the weathering of local schist and marble (Allen et al., 2001; Darmody et al., 2000; Thorn et al., 2001). Long-term experiments in Kärkevagge have also quantified chemical weathering rates on common rock types (Thorn et al., 2006, 2002). In mountain settings, the formation of vermiculite and smectite was confirmed for alpine soils in the Cascade Range of Washington, USA (Reynolds, 1971). Similarly, evidence that mica schist is weathering in conjunction with the accumulation of organic matter was reported for the formation of alpine soils in the northern Appalachians of Vermont, USA (Munroe, 2008; Munroe et al., 2007). Some of the most detailed research on clays in mountain soils has occurred in the European Alps where investigations of soil chronosequences have revealed rates of clay mineral formation (Egli et al., 2011, 2003), identified likely precursor minerals for pedogenic smectite (Egli et al., 2001b), and quantified losses of mobile elements during pedogenesis (Egli et al., 2001a). Globally, a comprehensive literature review has summarized climatic conditions under which different clay minerals are found in association with periglacial blockfields and other non-periglacial sites (Goodfellow, 2012). From this work, it is clear that clay minerals, including smectite, are present in many periglacial soils and regoliths, and that some of these clays have formed during chemical weathering associated with pedogenesis.

The majority of prior studies, however, focused on locations where the bedrock contains abundant, weatherable primary minerals such as feldspars and micas (e.g. Darmody et al., 2001; Dixon and Thorn, 2005; Dosseto et al., 2012; Egli et al., 2014, 2004; Thorn et al., 1989). In contrast, much less attention has focused on the clay content of soil and regolith in periglacial settings with more resistant lithologies. Thus it is less clear if neoformed clays are present in these environments, and if so, which clays are forming and from what precursor minerals.

* Corresponding author.
E-mail address: jmunroe@middlebury.edu (J.S. Munroe).

https://doi.org/10.1016/j.catena.2021.105324
Received 21 August 2020; Received in revised form 27 January 2021; Accepted 16 March 2021
Available online 31 March 2021

The Uinta Mountains of northeastern Utah are an interesting location in which to fill this knowledge gap (Fig. 1). The bedrock forming this prominent sub-range of the Rocky Mountain system is an assemblage of siliciclastic rocks (Dehler et al., 2007; Sears et al., 1982). The highest summits in the Uinta Mountains (hereafter, the "Uintas") reach elevations > 4 km above sea level, where long-term records indicate that mean annual air temperatures are < -2.0 °C, and mean annual precipitation is > 800 mm (Munroe, 2006). Together the combination of resistant, quartz-dominated bedrock and a rigorous periglacial climate could support the expectation of minimal chemical weathering and a corresponding lack of clay minerals.

In reality, however, soil and regolith in the alpine zone of the Uintas are notably rich in clay minerals (Munroe et al., 2015). This situation has been recognized since at least the early 1960′s when field descriptions of soil pedons in association with sorted stone polygons at an elevation > 3650 m noted the presence of "heavy silty clay loam" and other clay-rich soil horizons (Olson, 1962). Similarly, soil profiles described in association with an active frost boil at a slightly lower elevation were noted to contain "sticky, plastic, sandy clay loam" and "very sticky, plastic, silty clay". In both locations, the presence of clay films on ped faces was also reported (Olson, 1962). These early observations, corroborated by more recent studies, raise the question "What is the origin of the clays in these soils and surficial materials?"

In the case of the Uintas, there are at least two possible sources for clay minerals other than weathering of the local bedrock. First, a long-running network of samplers has established that eolian dust is a significant input to this mountain environment (Munroe, 2014; Munroe et al., 2019, 2015). An obvious long-term effect of this dust deposition is a prominent textural discontinuity present in nearly all soil profiles, where a silt-rich surface horizon abruptly overlies a sandier subsoil (Bockheim and Koerner, 1997; Munroe, 2007; Munroe et al., 2015). Similar features have been noted elsewhere in the Rocky Mountains (e.g. Dixon, 1991; Muhs and Benedict, 2006). Because the alpine zone of the Uintas was above the reach of erosive glacial ice during the Pleistocene (Munroe, 2006; Munroe and Laabs, 2009), these soils have been forming over Quaternary timescales, and perhaps longer. Thus, it is possible that the clay minerals in the Uinta alpine zone have formed through chemical weathering of eolian sediment over timescales in excess of 10^6 years.

The Uinta Mountain region was also impacted by volcanic ash deposition during the Neogene related to eruptions in the Basin and Range province to the west. Isotopic evidence suggests that the Uinta Mountains were uplifted to an elevation > 3 km by the Eocene (Norris et al., 1996), and the erosional surface beveled across the Uinta ridgecrest had apparently formed by the Oligocene (Bradley, 1936). Volcanic ash layers preserved in sedimentary rocks on the south flank of the Uintas date to ~ 30 Ma (Best et al., 2013; Kowallis et al., 2005). Given that the Uintas existed as a mountain range at the time of these eruptions, it is possible that some ash deposited on parts of the gently sloping Uinta ridgecrest remains there today. Weathering of this material under changing climatic regimes over the past ~ 30 Ma could also be responsible for at least some of the clay minerals present in modern soils.

Determining the origin of these clay minerals has implications beyond just a better understanding of processes operating in the critical zone of the Uintas, defined as the "*dynamic interface between the solid Earth and its fluid envelopes*" (National Research Council, 2001). Clays, as is widely recognized, play an essential role in soil fertility through their ability to hold and release cations that serve as plant available nutrients (e.g. Velde and Meunier, 2008). This same characteristic also makes clays important for immobilizing metals and other contaminants (Bradl, 2004), and for neutralizing acidic precipitation via cation exchange (April et al., 1986). Better understanding of which clay minerals are present in alpine environments, what their precursors were, and how they form would improve geoecological models of how mountain ecosystems evolve, and predictions of how they may change in the future. Furthermore, by virtue of their adhesion, the presence or absence of clay minerals is an important control on soil erodibility (Grissinger, 1966). Certain expandable clays, which swell and shrink in response to hydration and dehydration, also contribute to surface disturbance with further connections to erosion (Freebairn et al., 1996). Enhanced knowledge of clay minerals in alpine soils, therefore, would inform management decisions involving grazing and recreation that contribute to erosional impacts in mountain environments (Alewell et al., 2015). Finally, due to the common association of different clay minerals with specific temperature and precipitation conditions, clays are significant sources of paleoclimate information (e.g. Charbonnier et al., 2020; Singer, 1984, 1980; Spinola et al., 2017). Long-term climate records can be difficult to find in high-mountain environments above the glacial limit, and as a result, clay minerals can be important in locations where no other paleoclimate records are available.

This project was designed to test the hypothesis that the clay minerals in the alpine critical zone of the Uinta Mountains are not derived from the local bedrock, but rather reflect weathering of volcanic ash under different climatic conditions beginning in the Oligocene, and weathering of eolian sediment over Quaternary timescales, perhaps longer. A field area was selected where visibly altered, clay-rich material outcrops at the top of cirque headwalls (Fig. 2). These exposures provide a window into material present a few meters below the modern ground surface – depths that are inaccessible to hand excavation, and therefore

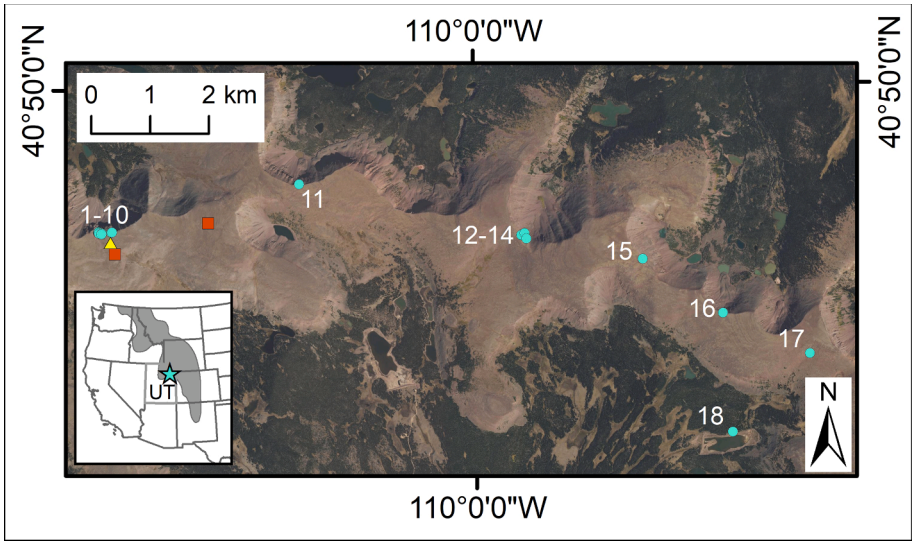

Fig. 1. Location map of the study area in northeastern Utah, USA (inset, star), and locations of samples C-1 through C-18 (blue circles) displayed over a true color satellite image of the eastern Uinta Mountains (US National Agricultural Imagery Program, WGS-84, UTM Zone 12 N). The location of the Dust-1 dust sampler is indicated by the yellow triangle, and the positions where rock samples were gathered are noted by red squares. The reddish color of the Uinta bedrock is obvious in the above-treeline landscape where most samples were collected. (For interpretation of the references to color in this figure legend, the reader is referred to the web version of this article.)

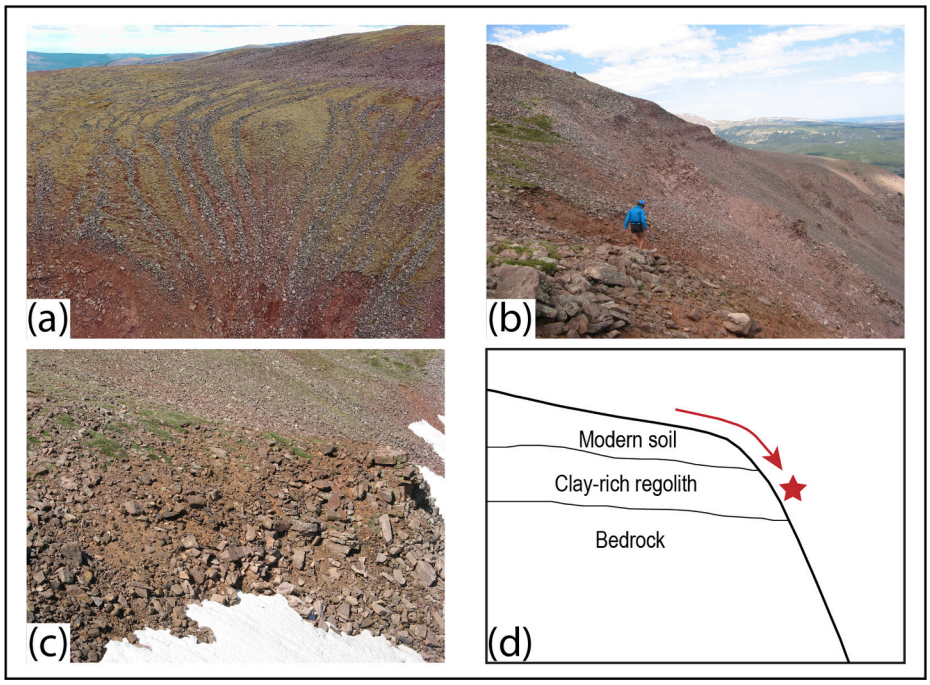

Fig. 2. Example photographs of typical exposures of the sampled materials. (a) Oblique aerial photograph showing the characteristically reddish-orange, clay-rich material outcropping at the top of the cirque headwall where samples C-3 through C-5 were collected. Periglacial stone stripes delivering regolith downslope to the lip of the headwall are clearly visible. (b) Descending over the lip of the headwall to collect sample C-3. (c) Ground-level view of weathered, orange-brown sediment outcropping at site C-1. (d) Schematic cross-section illustrating the relative position of the modern soil profile (immediately beneath the ground surface), the clay-rich regolith that is the focus of this study (beneath the modern soil profile), and the deeper bedrock. Red arrow signifies that samples of the regolith (star) were collected by rappelling over the lip of the cirque headwall to reach exposures that provided access to the clay-rich regolith that would otherwise have been too deep to sample by hand excavation. (For interpretation of the references to color in this figure legend, the reader is referred to the web version of this article.)

have remained unexplored in previous investigations that focused on modern soil profiles. These materials were collected and analyzed with a variety of mineralogical and geochemical techniques. Results were compared with analyses of local bedrock and modern dust to test the theory that these materials formed through weathering of older volcanic ash, and younger alpine loess.

2. Study area

The Uinta Mountains of northeastern Utah, USA provide an ideal location in which to consider the effects of long-term chemical weathering and dust deposition in a periglacial, alpine critical zone underlain by resistant bedrock (Fig. 1). During the Laramide Orogeny in the early Paleogene, the Precambrian siliciclastic rocks of the Uintas were deformed into an asymmetric, doubly plunging anticline, the axis of which essentially coincides with the topographic crest of the mountain range (Dehler et al., 2007; Hansen, 1986; Sears et al., 1982). Stratigraphic layers, therefore, dip gently southward on the south flank of the range, more steeply to the north on the north flank of the range, and are nearly flat beneath the ridge crest (Bradley, 1936). Repeated alpine style glaciation during the Quaternary excavated deep glacial valleys, however glaciers only locally coalesced across the higher interfluves (Munroe and Laabs, 2009). As a result, particularly the eastern half of the glaciated Uintas is characterized by an extensive, periglacial landscape that was above the reach of erosive ice during the Pleistocene (Munroe, 2006). This “summit flat” is a continuation of an extensive geomorphic feature known as the Gilbert Peak erosion surface that was produced by lateral planation by rivers draining from the uplifting Uintas (Bradley, 1936). Today this landscape is above treeline and features gentle slopes mantled by alpine tundra. In many places, areas of vegetation are interspersed with well-developed, fossil patterned ground features (Fig. 2) including sorted polygons and stone stripes (Munroe, 2007). Smaller non-sorted features including frost boils are also common and are apparently active under the modern climate.

A considerable body of prior work has focused on soils in the Uinta Mountains (Bockheim et al., 2000, 2000; Bockheim and Koerner, 1997; Munroe, 2007; Munroe et al., 2020, 2015). In the alpine zone specifically, soil profiles typically contain a dark brown, organic-rich A horizon developed in silty loess, which disconformably overlies a series of lighter, redder, sandier, 2B horizons developed in locally derived regolith. Most of these are 2Bw horizons, but some contain cutans and sufficient translocated clay to be classified as 2Bt horizons. Granular structure is common in A horizons, whereas platy structure related to freeze thaw is common in Bw horizons, and subangular blocky structures are present in horizons with higher clay content. Most profiles exhibit evidence for cryoturbation and horizon distortion related to solifluction. This includes broken horizon boundaries, discrete inclusions of organic matter at depth within the solum, and irregularly shaped pockets of coarse sand and gravel. No hand excavations have penetrated to $>$ 100 cm in these soil profiles, thus it is unclear whether permafrost and gelic materials are present within 200 cm of the surface. As a result, Uinta alpine soils are provisionally classified with the assumption that they lack permafrost (Munroe, 2007). In US Soil Taxonomy, soils with 2Bt horizons classify as Inceptic Haplocryalfs. Soil profiles with particularly thick and organic-rich A horizons classify as various types of Cryolls. Profiles with lower clay content and typically minimal development classify in the order Inceptisols.

3. Methods

3.1. Field methods

Fieldwork for this project in August 2016 focused on collecting a representative suite of clay-rich samples from the periglacial upland at the eastern end of the alpine zone in the Uinta Mountains. Most (n = 16) of these samples were collected from exposures along the headwall defining the northern boundary of the summit flat (Fig. 1), exposures that provide access to the materials underlying the stony mantle of cryoturbating regolith and soil forming the summit flat surface (Fig. 2d). For simplicity, the sampled material is referred to as “soil”, but it is important to note that this sediment is positioned stratigraphically below the modern soil profile (Fig. 2d). Samples were collected by hand after rappelling over the lip of cirque headwalls. Another clay-rich sample was collected from a hand excavation into the summit flat surface away from the lip of the headwall. A final sample, representing material that was transported down from the summit flat, was collected from clay-rich material on the floor of the glacial valley south of the ridge crest. Because they were accessed by digging vertically down from

the ground surface, the last two samples are from B horizons in the modern soil profile. Together, 18 clay-rich samples were collected and analyzed (Fig. 1).

The bedrock of the study area is mapped as the Hades Pass unit of the Uinta Mountain Group, described as grayish-red, brownish-red, and whitish-gray quartz sandstone, arkose and shale (Bryant, 2010; Wallace, 1972). Representative rock samples (n = 6) were collected from the ground surface and shallow excavations at two locations (Fig. 1). Along with samples (n = 4) previously collected in other parts of the eastern Uinta Mountains, these provide a total of 10 samples yielding a general perspective on the properties of the Uinta Mountain bedrock.

Properties of modern dust deposited in the Uinta Mountains are constrained by a network of passive dust samplers (Munroe, 2014; Munroe et al., 2020). Eight collectors (Dust-1 through Dust-8) are deployed across the Uinta range; one of these (Dust-1) is located in the study area for this project (Fig. 1). Prior analysis of the mineralogy and geochemistry of the material collected by these samplers (n = 54 samples) reveals that dust mineralogy and geochemistry is extremely consistent from site to site and from year to year (Munroe, 2014; Munroe et al., 2015).

3.2. Laboratory methods

All soil and rock samples were subjected to a series of analyses to characterize their physical and chemical properties. As preparation for grain size analysis, ~10-g aliquots of each sample were reacted with 20 mL of 35% hydrogen peroxide at room temperature. An additional 10 mL of peroxide was added after 3 days, and the entire volume was left to react for approximately one week. Peroxide was then diluted with distilled water and the samples were centrifuged, decanted, rinsed with distilled water, and centrifuged/decanted a second time. Sodium hexametaphosphate (20 mL, 3%) was added and the samples were capped and mixed once more. After from 1 to 3 days contact time with the dispersant, the grain size distribution of each sample was measured through laser scattering in a Horiba LA-950 equipped with an autosampler. This instrument has an effective range from 50 nm to 3 mm, and a refractive index of 1.54 and an imaginary component of 0.1i were employed in calculating the grain size distribution. A subset (10%) of samples were rerun as duplicates, and the analyzer was checked before and after each run with in-house standards.

Because this investigation focused on the origin and properties of fine material in these soils, the clay fraction (<2 μm) was separated through settling. Approximately 100 mg of sample was placed in a 250-mL beaker and slaked in 100 mL of distilled water for ~ 1 week. Samples were stirred once each day with a glass rod. After samples were completely disaggregated, they were sonified for 60 s and poured into Atterberg cylinders with additional distilled water. After a 3 hr and 53 min settling time calculated from Stokes Law, the supernatant containing the < 2 μm fraction was decanted. The grain size distribution of this supernatant was analyzed immediately in the Horiba to confirm successful separation of the clay fraction. A small amount of each sample was removed with an eyedropper and dried on a glass slide to produce oriented samples for x-ray diffraction analysis. Samples were then frozen overnight, and dried in a Labconco Freezone freeze dryer for 48 h. Dried samples were homogenized to a fine powder in an agate mortar and pestle.

Homogenized samples were briefly reconstituted to a paste-like consistency with the addition of a small amount of distilled water. The resulting paste was smeared onto a watch glass and covered with clear plastic wrap. The color of this paste was then measured with a Konica-Minolta CM-2600D color spectrophotometer. The resulting color was described in the cieLAB system, as well as in terms of cumulative reflectance in 10-nm bands from 360 to 740 nm. These values were also converted to pseudo-Munsell format for comparison with previously reported soil colors.

After color determination, samples were oven dried and ignited at 1000 °C for 1 h in a Leco TGA-701 thermogravimetric analyzer. The percent loss on ignition was determined from the starting dry mass and the final ignited mass. Ignited samples were added to a platinum crucible in a 1:10 ratio of sample to lithium metaborate flux, melted in a Claise LeNeo autofluxer to produce a glass disk, and analyzed through x-ray fluorescence in a Thermo ARL Quant'X EDXRF to determine major element composition. USGS standard RGM-1 (silica-rich rhyolite) was run with each batch of 9 samples to ensure consistency. Resulting major element abundances, reported in oxide weight percent, were adjusted given measured loss on ignition values. These adjusted values were used as inputs in calculating the chemical index of alteration (Harnois, 1988). Oxide values were also converted to atomic abundances for consistency with trace element abundances determined through ICP-MS analysis at SGS Minerals following methods GE-ICP91A50 and GE-ICM40B.

Scanning electron microscope with energy dispersive x-ray spectrometry (SEM-EDS) analyses were performed on carbon-coated mineral powders (<2-μm fraction, unpolished) using a Tescan Vega 3 LMU SEM with EDS & EBSD attachments. Operating parameters included 20 kV with a working distance of 15 mm and spot size for EDS analysis of 0.2 μm. Compositions of clay minerals determined by EDS are presented as molar values on a $O_{10}(OH)_2$ basis.

The mineralogy of the clay fraction of each sample was analyzed using x-ray diffraction (XRD) in a Bruker D-8 diffractometer with CuKα radiation, theta compensating slits, and a graphite monochromator. Each sample was scanned from 2 to 40°, with step size and time of 0.02° and 1 s. Slides were reanalyzed after treatment with ethylene glycol.

To explore combinations of layer types associated with XRD data, diffraction patterns were modeled with Newmod II < http://www.newmod-for-clays.com/>. Evidence for interstratified clays is described below, most notably peak broadening and peak positions that are typical of interstratified clays with kaolinite, illite and/or smectite layer types (Moore and Reynolds, 1997). Experimental parameters were: smectite contained Ca as an interlayer cation and 0.5 Fe per 2:1 layer (based on SEM observations) with a d(001, EG) = 17.0 Å; illite was defined as containing 0.8 K and 0.4 Fe per 2:1 layer (based on SEM observations) with a d(001) = 10.0 Å. Crystallite thickness was set to N = 2–6 to match peak broadening observed in XRD patterns associated with clays that show evidence of interstratification. The one exception is discrete kaolinite, for which thickness was set to N = 5–15. Following standard nomenclature for interstratified clays (Moore and Reynolds, 1997) the layer type with the smallest d-spacing is listed first with its decimal abundance, followed by the layer type(s) with larger d-spacing. These are preceded by a variable "R" indicating ordering, from random stacking of layer types (R0) to ordered stacking arrangements where layer types tend to occur in packets of 1:1 (R1) or 3:1 (R3). As an example, "R0 kaolinite(0.4)-smectite" signifies randomly interstratified layers of kaolinite (40%) and smectite (60%) within a given crystal of clay.

4. Results

4.1. Color and grain size distribution

Colorimetric analysis of the < 2-μm fraction of the 18 samples confirms the relatively strong orange colors noted in the field. Values of a* are all positive, with a mean of 12.9, indicting a strong red tone (Table 1). Values of b* average 16.1, indicating a large component of yellow. In continuous analysis of wavelengths from 360 to 740 nm, all samples are strongly reflective in the range corresponding to orange-red (Fig. 3a). In Munsell color space, all samples have YR hues (yellow–red), typically around 4YR. Munsell values average 4.2, and chromas average 3.5. For reference, the official Munsell color 5YR 4/4 is "reddish brown".

These samples were collected because they appeared distinctly fine-grained in the field, and grain size analysis with laser scattering confirms that assessment. The overall mean grain size of these bulk samples is 43.3 μm, with a median of 12.7 μm (Table 1). Bulk grain size

Table 1
Color and Grain Size Data for Clay Samples.

		C-1	C-2	C-3	C-4	C-5	C-6	C-7	C-8	C-9	C-10	C-11	C-12	C-13	C-14	C-15	C-16	C-17	C-18	Average
Dom. Mineral	–	smectite	smectite	smectite	smectite	illite	smectite	illite	illite	illite	illite	smectite	illite	smectite	illite	smectite	illite	illite	smectite	–
Hue	–	4.1YR	4YR	3.4YR	2.8YR	2.6YR	3.8YR	4.8YR	4.6YR	4.1YR	5.3YR	2YR	2.9YR	7.7YR	3.2YR	3.4YR	3.2YR	6.8YR	5.8YR	–
Value	–	5.2	4.5	4.6	4.4	3.8	3.9	4.6	4.2	4.2	3.4	4.2	4.3	5.3	3.7	4.3	3.8	3.4	3.8	4.2
Chroma	–	4.1	3.4	4.4	3.7	2.5	4.4	3.9	4.0	3.1	3.5	3.7	4.4	3.0	4.3	4.0	2.9	2.1	2.5	3.5
L*	–	53.1	46.4	46.4	45.3	38.6	39.3	46.9	42.7	43.2	34.5	42.8	43.9	54.2	37.7	43.6	39.1	34.6	39.2	42.9
a*	–	14.0	12.2	15.8	14.2	10.3	16.4	13.4	14.2	11.6	12.4	14.8	16.7	8.0	16.5	14.9	11.8	7.0	8.9	12.9
b*	–	18.6	15.3	19.0	15.4	10.2	19.9	18.9	18.9	14.3	17.1	14.3	18.7	16.2	18.5	17.5	12.7	10.8	12.7	16.1
Mean	μm	43.7	44.6	51.9	39.5	91.4	43.1	26.3	24.8	34.3	89.5	55.7	37.4	42.2	30.7	31.6	39.2	43.2	10.8	43.3
Median	μm	8.9	8.4	5.8	9.6	51.5	6.8	4.1	3.6	9.0	27.9	10.9	11.4	14.8	6.0	12.1	16.1	19.2	3.0	12.7
Std. Dev.	μm	68.8	72.3	90.8	65.4	102.2	75.2	50.6	50.5	59.8	121.1	119.6	58.9	57.3	57.9	45.6	56.1	60.0	21.9	68.6
Coarse Sand	%	0.0	0.0	0.0	0.0	0.3	0.0	0.0	0.0	0.0	1.1	1.9	0.0	0.0	0.0	0.0	0.0	0.0	0.0	0.2
Med Sand	%	2.4	2.9	5.9	2.1	8.8	3.5	0.8	0.9	1.7	10.8	3.1	1.5	1.2	1.6	0.4	1.4	1.8	0.1	2.8
Fine Sand	%	10.2	10.4	11.9	9.3	19.5	9.8	5.2	4.7	7.3	15.3	7.5	7.6	8.9	6.2	5.6	7.1	8.0	0.6	8.6
Very Fine Sand	%	11.4	10.6	6.4	8.0	16.8	8.2	7.6	7.1	6.9	10.2	9.7	9.8	12.6	6.9	9.8	10.0	10.8	1.7	9.1
Coarse Silt	%	9.7	8.4	4.4	8.3	14.4	7.8	9.6	9.0	10.6	11.6	10.1	12.7	11.3	10.0	10.3	15.7	17.6	8.2	10.5
Medium Silt	%	8.6	8.9	5.1	12.2	12.5	8.0	8.1	6.3	13.3	13.1	11.9	14.0	17.8	10.5	18.1	19.8	20.3	11.1	12.2
Fine Silt	%	11.8	12.1	12.2	20.0	10.6	12.1	10.3	9.8	15.9	12.1	17.0	14.0	26.2	12.2	28.9	18.1	14.6	13.3	15.1
Very Fine Silt	%	18.5	18.8	22.0	29.3	12.1	18.4	18.2	20.6	22.2	15.3	22.8	18.0	20.5	17.4	25.0	20.5	15.0	20.2	19.7
<2um	%	27.4	28.0	32.1	10.9	5.0	32.2	40.2	41.5	22.0	10.6	16.0	22.4	1.4	35.1	1.9	7.4	11.9	44.8	21.7
%Sand	%	24.0	23.9	24.2	19.4	45.4	21.5	13.7	12.8	15.9	37.3	22.2	18.9	22.7	14.7	15.8	18.6	20.7	2.4	20.8
%Silt	%	48.7	48.1	43.7	69.7	49.6	46.3	46.1	45.8	62.1	52.0	61.8	58.7	75.9	50.2	82.3	74.1	67.5	52.8	57.5
%Clay	%	27.4	28.0	32.1	10.9	5.0	32.2	40.2	41.5	22.0	10.6	16.0	22.4	1.4	35.1	1.9	7.4	11.9	44.8	21.7

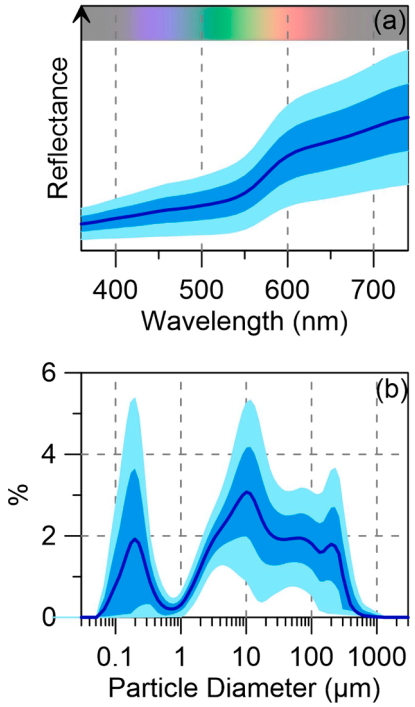

Fig. 3. (a) Reflectance of samples C-1 through C-18 (<2 μm fraction) displayed as overall average (dark blue line), ±1-σ (medium blue), and ± 2-σ (light blue). Samples are strongly reflective at wavelengths corresponding to orange-red. (b) Bulk grain size distribution of samples C-1 through C-18 displayed as overall average (dark blue line), ±1-σ (medium blue), and ± 2-σ (light blue). Samples have modes of ~ 200 μm (fine sand), 10 μm (fine silt), and 0.2 μm (colloid). (For interpretation of the references to color in this figure legend, the reader is referred to the web version of this article.)

distributions (Fig. 3b) exhibit three modes: ~200 μm (fine sand), ~10 μm (fine silt), and ~ 0.2 μm (colloid). In half of the samples, the < 2-μm material is more abundant than very fine silt, up to a factor of 2.2 × . Overall, the abundance of sand (2 mm to 63 μm), silt (63 to 2 μm), and clay (<2 μm) in bulk samples averages 20.8%, 57.5%, and 21.7% respectively, corresponding to a silt loam texture. For comparison, modern dust landing in the alpine zone of the Uintas is 31% very fine silt, with an average abundance of < 2-μm material of 8% (Munroe et al., 2015).

4.2. Geochemical characterization

XRF analysis reveals that Si and Al are the most abundant major elements in these samples, followed by Fe, K, and Mg. All other major elements average < 1% (Fig. 4a). The mean loss-on-ignition of these samples is 11.9%, indicating the presence of interstitial water, structural water (OH in clays or hydroxides), and organic matter.

Analysis with ICP-MS (Table 2) reveals that five trace elements are present at average abundances > 100 ppm: Ba (481 ppm), Zr (242 ppm), Sr (116 ppm), Rb (113 ppm), and V (103 ppm). When these abundances are normed to mean values in the upper continental crust (Wedepohl, 1995), several elements have abundances > 2 × normal (Fig. 4b). These include As (4.5 ×), W (4.0 ×), Sb (2.9 ×), Li (2.4 ×), and Cu (2.2 ×). In contrast, 12 elements have abundances below normal values for crustal rocks (Fig. 4b). These include the major elements Mg (0.9 ×), K (0.7 ×), P (0.6 ×), Mn (0.6 ×), Ca (0.2 ×), and Na (0.002 ×).

The chemical composition of the clay samples exhibits notable contrasts with samples of dust and local bedrock (Table 3). The abundance of Al, for instance, is much higher in the clays (10.7%) than in dust (7.1%) or bedrock (2.7%). A similar pattern is seen in Fe, and REEs. In contrast, the average abundance of P, Pb, Sb, Sn, and Sr is highest in

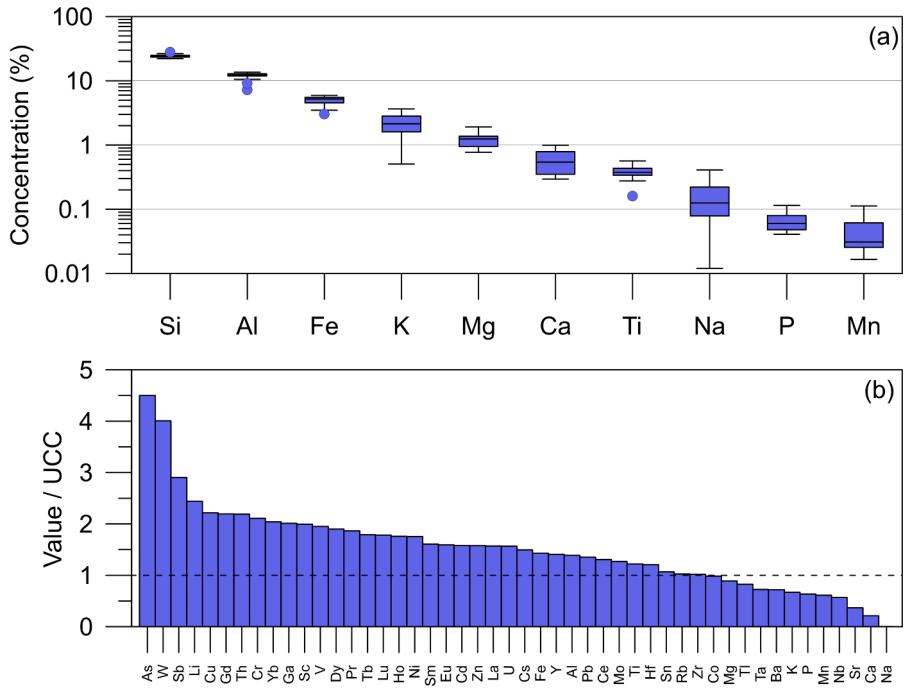

Fig. 4. Geochemistry of the < 2-μm fraction of samples C-1 through C-18. (a) Abundance of major elements presented as atomic concentrations (in wt %). (b) Ratio of atomic abundance relative to the average composition of upper continental crust (Wedepohl, 1995).

dust. Co, Hf, W, and Zr are most abundant in rock samples. Ratios of immobile elements, such as Ti, Zr, and the REEs, are similar for clays and dust samples, and in most cases diverge notably from ratios in rock samples (Fig. 5).

4.3. Mineralogy

XRD analysis of clay fractions indicates the occurrence of three main layer types: an expandable 2:1 layer type (referred to hereafter as "smectite"), a 10 Å non-expandable 2:1 layer type (referred to as "illite"), and a 7 Å 1:1 layer type (referred to as "kaolinite"). Samples can be divided into three mineralogical groups, with two end members and one mixture.

Smectite End-Member: The smectite end member is best illustrated by sample C-3, which presents a sharp and symmetrical 15.1 Å peak in the air-dried state that expands to 17.1 Å when solvated with ethylene glycol (EG) (Fig. 6). The 00*l* peaks for C-3 in the EG state occur at 8.51, 5.58, 4.2 (broad) and 3.34 Å – this nearly rational (integer multiple) relationship indicates predominance of stacks of 17 Å 2:1 layers with a two-layer EG structure in the interlayer (Moore and Reynolds, 1997). This relationship also indicates little interstratification of illite or kaolinite layer types.

Illite-Kaolinite End-Member: Samples C-14 and C-16 typify the illite-kaolinite end member, where kaolinite is identified by 00*l* peaks at 7.17 and 3.57 Å that only minimally shift position or shape with EG, and illite by 00*l* peaks at 10.2, 5.02 and 3.34 Å that change minimally with EG solvation (Fig. 6). These attributes indicate occurrence of at least some of the kaolinite and illite as relatively homogeneous packets of kaolinite or illite layer types, whether within crystals or whether as individual crystals of kaolinite and illite. It is notable, however, that the illite 001 peak is centered at 10.2 Å and is asymmetrical towards the low-angle side, indicative of interstratified layer types within an illite-dominated crystal. The presence of relatively weak peaks and elevated background intensity between 20 Å and 11 Å indicate the presence of 2:1 smectite-like layers with variable interlayer thickness and likelihood of interstratified kaolinite and/or illite layers (Moore and Reynolds, 1997).

Interstratified Clay Minerals: Nearly all samples exhibit XRD evidence for interstratified clays. Aside from end-member smectite in sample C-3 (with its sharp 17.1 Å 001 peak), the 001 peaks for expandable clays in these samples are broader and tend to occur in the 17.5 to 18.8 Å range. Furthermore, the higher-order 00*l* peaks (002, 003 etc.) are irrational (non-integer) for all samples containing a strong peak in the 17.5–18.8 Å range. Sample C-1 is a good example of irrational 00*l* peaks, with a d(0 0 1) spacing of 18.8 Å, a d(0 0 2) of 8.34 Å, a broad 003 centered at ~ 5.6 Å, and an asymmetric (towards low angle) broad peak at ~ 26.6 °2Θ with local peaks of 3.38 and 3.34 Å (Fig. 6). This pattern suggests the occurrence of smectite-like 2:1 layers randomly interstratified with illite-like 2:1 layers and/or kaolinite-like 1:1 layers, forming either two-component or three-component interstratified minerals (Hong et al., 2015; Reynolds and Hower, 1970; Ryan et al., 2016). On the other hand, some samples (e.g. C-11, C-14 and C-16) exhibit relatively sharp kaolinite and illite peaks that change only minimally when EG-saturated (Fig. 6), suggesting localized occurrence of sufficiently thick stacking domains of discrete kaolinite or illite within crystals. Absence of superlattice peaks indicates a lack of ordering in the interstratified clays, suggestive of random stacking of layer types in these clays (Moore and Reynolds, 1997).

Overall, the clay mineralogy of these samples exhibits a range of compositions (Fig. 7), from nearly pure smectite (C-3); to compositions that represent mixtures of kaolinite, illite and smectite, at times with relatively high amounts of smectite (e.g. C-1, C-2, C-4, C-6, C-11, C-13, C-18); to clay fractions dominated by illite and kaolinite (e.g. C-12, C-5, C-14, C-16). In contrast, local bedrock is dominated by quartz with small amounts of mica and chlorite occurring in shale beds (Fig. 7). Similarly, the mineralogical signature of dust (Fig. 7) includes mica, chlorite and quartz, plus plagioclase and potassium feldspar and small amounts of kaolinite (Munroe, 2014; Munroe et al., 2015).

4.4. Clay composition and stoichiometry

SEM-EDS analysis indicates a near-absence of end-member crystals of kaolinite, illite or smectite. Out of 111 clay-like crystals or clasts probed, none were discrete kaolinite, one was close to illite [from weathered K-feldspar in sample C-11: $(K_{0.82}Ca_{0.05})$ $(Al_{1.42}Fe_{0.37}Mg_{0.13})$

Table 2
ICP-MS Results for Clay Samples.

	Limit	Unit	C-1	C-2	C-3	C-4	C-5	C-6	C-7	C-8	C-9	C-10	C-11	C-12	C-13	C-14	C-15	C-16	C-17	C-18
Al	0.01	%	13.1	12.4	11.5	11.8	2.5	13.2	11.7	12.8	13.0	4.2	12.0	6.6	12.8	13.3	12.1	12.4	5.3	12.9
As	5	ppm	13.0	14.0	13.0	15.0	2.5	11.0	15.0	15.0	17.0	6.0	2.5	2.5	2.5	2.5	9.0	9.0	2.5	10.0
Ba	10	ppm	342.0	373.0	342.0	475.0	210.0	358.0	501.0	504.0	636.0	334.0	462.0	425.0	530.0	272.0	652.0	725.0	442.0	1067.0
Ca	0.1	%	1.0	0.9	1.1	0.7	0.1	0.7	0.5	0.4	0.6	0.2	0.5	0.3	1.1	1.0	0.4	0.5	0.3	0.9
Cd	0.2	ppm	0.1	0.1	0.1	0.1	0.1	0.1	0.1	0.1	0.4	0.1	0.1	0.3	0.2	0.1	0.1	0.2	0.1	0.5
Ce	0.1	ppm	55.8	70.9	77.7	115.0	27.3	91.3	67.9	104.0	134.0	53.5	88.5	75.3	114.0	64.3	109.0	155.0	56.4	86.6
Co	0.5	ppm	8.2	9.1	10.6	14.9	3.4	11.3	8.8	10.4	17.0	8.1	12.3	12.7	10.0	6.0	15.2	23.0	9.1	15.8
Cr	10	ppm	79.0	85.0	73.0	96.0	29.0	110.0	80.0	90.0	86.0	39.0	100.0	54.0	24.0	29.0	89.0	110.0	47.0	109.0
Cs	0.1	ppm	10.6	11.2	9.3	8.7	1.4	11.0	11.9	11.9	12.9	3.9	6.8	5.3	4.2	6.4	9.7	12.3	4.6	14.0
Cu	10	ppm	40.0	36.0	32.0	43.0	5.0	43.0	25.0	33.0	42.0	12.0	37.0	19.0	33.0	74.0	27.0	24.0	12.0	34.0
Dy	0.05	ppm	7.3	5.7	5.4	6.5	1.6	6.8	5.6	6.2	7.4	3.1	3.3	4.9	8.3	6.4	6.1	6.1	3.4	5.1
Er	0.05	ppm	3.8	3.3	3.2	3.7	1.1	3.9	3.3	3.5	4.0	1.7	1.7	3.0	4.9	3.8	3.4	3.3	2.0	3.0
Eu	0.05	ppm	2.0	1.4	1.3	1.8	0.4	1.8	1.3	1.5	2.1	0.8	1.4	1.1	2.9	1.9	1.7	1.9	0.9	1.2
Fe	0.01	%	5.7	5.4	5.5	5.6	1.0	5.1	5.2	5.7	5.9	2.1	3.9	2.9	3.2	3.8	5.2	5.5	2.3	5.6
Ga	1	ppm	33.0	32.0	31.0	32.0	7.0	36.0	29.0	31.0	34.0	11.0	32.0	17.0	30.0	33.0	33.0	35.0	14.0	37.0
Gd	0.05	ppm	8.4	6.1	5.6	7.3	1.5	7.7	5.7	6.7	8.4	3.4	4.9	4.9	9.7	7.6	6.9	7.4	3.6	5.0
Hf	1	ppm	6.0	7.0	6.0	11.0	10.0	8.0	8.0	8.0	5.0	7.0	2.0	13.0	5.0	7.0	5.0	6.0	7.0	5.0
Ho	0.05	ppm	1.4	1.2	1.1	1.3	0.3	1.3	1.1	1.2	1.5	0.6	0.6	1.0	1.7	1.3	1.2	1.2	0.7	1.1
K	0.1	%	1.4	1.7	1.2	2.2	1.2	2.1	1.8	2.0	2.2	1.2	3.3	1.8	1.0	0.7	3.0	3.4	1.8	2.6
La	0.1	ppm	73.1	52.9	47.5	60.2	15.6	66.0	43.4	52.5	66.1	27.1	49.0	32.4	76.6	50.7	57.6	69.4	28.8	44.1
Li	10	ppm	58.0	54.0	60.0	62.0	5.0	46.0	64.0	67.0	80.0	27.0	54.0	32.0	55.0	74.0	50.0	61.0	33.0	84.0
Lu	0.05	ppm	0.6	0.5	0.6	0.6	0.2	0.6	0.5	0.6	0.6	0.3	0.2	0.5	0.7	0.6	0.5	0.5	0.3	0.4
Mg	0.01	%	1.6	1.6	1.8	1.4	0.2	1.4	0.9	0.9	1.3	0.4	1.1	0.5	1.9	2.0	1.0	1.4	0.6	1.8
Mn	10	ppm	233.0	228.0	238.0	461.0	62.0	162.0	199.0	223.0	782.0	411.0	125.0	414.0	549.0	231.0	274.0	546.0	323.0	339.0
Mo	2	ppm	3.0	1.0	1.0	1.0	1.0	1.0	3.0	3.0	3.0	1.0	2.0	1.0	1.0	1.0	2.0	4.0	1.0	2.0
Nb	1	ppm	18.0	18.0	18.0	16.0	5.0	19.0	22.0	23.0	17.0	7.0	6.0	10.0	15.0	17.0	16.0	16.0	12.0	12.0
Nd	0.1	ppm	61.7	41.2	38.5	52.0	11.5	54.8	36.0	42.8	56.2	22.2	39.5	28.9	66.6	48.1	48.6	57.0	23.7	34.2
Ni	5	ppm	37.0	37.0	46.0	39.0	2.5	44.0	22.0	26.0	47.0	11.0	41.0	20.0	29.0	30.0	40.0	55.0	12.0	49.0
P	0.01	%	0.0	0.0	0.0	0.0	0.0	0.0	0.0	0.1	0.1	0.0	0.0	0.0	0.0	0.0	0.1	0.1	0.1	0.1
Pb	5	ppm	15.0	20.0	23.0	25.0	9.0	27.0	25.0	26.0	31.0	18.0	20.0	21.0	26.0	25.0	24.0	34.0	18.0	27.0
Pr	0.05	ppm	17.5	11.6	10.9	14.4	3.3	15.4	9.6	11.8	15.1	6.2	10.9	7.9	18.6	12.9	13.4	15.9	6.6	9.7
Rb	0.2	ppm	99.6	119.0	88.8	120.0	43.5	138.0	120.0	140.0	153.0	60.2	136.0	92.2	43.0	49.4	166.0	183.0	84.7	194.0
Sb	0.1	ppm	1.3	1.6	1.4	1.3	0.2	1.1	1.4	1.3	1.2	0.4	0.6	0.5	0.6	0.7	0.9	0.7	0.4	0.6
Sc	5	ppm	18.0	17.0	16.0	17.0	2.5	19.0	15.0	17.0	18.0	6.0	11.0	9.0	11.0	14.0	15.0	19.0	7.0	20.0
Sm	0.1	ppm	10.8	7.1	6.9	9.5	2.0	9.8	6.3	7.6	10.3	4.2	7.1	5.6	11.8	8.7	8.5	9.7	4.3	5.9
Sn	1	ppm	3.0	3.0	3.0	3.0	0.5	4.0	3.0	3.0	3.0	0.5	2.0	2.0	2.0	4.0	3.0	4.0	2.0	3.0
Sr	10	ppm	124.0	116.0	115.0	124.0	50.0	111.0	93.0	101.0	110.0	62.0	297.0	77.0	131.0	85.0	128.0	154.0	101.0	110.0
Ta	0.5	ppm	1.3	1.3	1.2	1.1	0.3	1.5	1.6	1.6	1.2	0.3	0.3	0.8	1.4	1.7	1.2	1.2	0.8	0.9
Tb	0.05	ppm	1.2	0.9	0.9	1.1	0.2	1.1	0.9	1.0	1.2	0.5	0.6	0.8	1.3	1.1	1.0	1.1	0.5	0.8
Th	0.1	ppm	21.6	21.5	22.5	25.6	5.7	25.7	20.9	25.2	23.3	9.3	22.9	14.0	57.9	26.3	23.9	29.5	11.7	18.6
Ti	0.01	%	0.4	0.4	0.4	0.5	0.2	0.4	0.6	0.6	0.4	0.2	0.2	0.3	0.3	0.3	0.5	0.5	0.4	0.4
Tl	0.5	ppm	0.6	0.6	0.7	0.8	0.3	0.8	0.8	0.8	0.8	0.3	0.7	0.3	0.5	0.3	0.8	0.9	0.3	1.1
Tm	0.05	ppm	0.6	0.5	0.5	0.6	0.2	0.6	0.5	0.5	0.6	0.3	0.2	0.5	0.7	0.5	0.5	0.5	0.3	0.4
U	0.05	ppm	3.3	3.3	3.0	4.2	1.6	4.0	5.4	6.0	5.4	2.4	2.7	4.1	3.4	4.1	5.1	4.8	3.0	4.7
V	5	ppm	111.0	121.0	108.0	136.0	28.0	115.0	133.0	144.0	140.0	58.0	94.0	67.0	65.0	62.0	124.0	137.0	61.0	156.0
W	1	ppm	2.0	2.0	4.0	4.0	4.0	3.0	2.0	3.0	2.0	9.0	2.0	1.0	10.0	8.0	6.0	31.0	6.0	2.0
Y	0.5	ppm	35.4	30.8	28.7	33.3	8.7	32.7	30.3	31.8	39.8	16.2	16.7	26.6	52.3	35.9	30.2	30.2	17.5	27.0
Yb	0.1	ppm	3.7	3.3	3.6	3.7	1.2	3.8	3.2	3.5	3.8	1.7	1.6	3.0	4.4	3.5	3.2	3.1	2.0	2.8
Zn	5	ppm	97.0	103.0	75.0	91.0	15.0	86.0	77.0	85.0	132.0	43.0	50.0	60.0	74.0	104.0	87.0	113.0	65.0	120.0
Zr	0.5	ppm	212.0	256.0	224.0	402.0	375.0	279.0	250.0	256.0	169.0	241.0	110.0	494.0	162.0	198.0	169.0	171.0	243.0	145.0

Table 3
ICP-MS Geochemistry of Clay, Rock, and Dust Samples.

		Clay (n = 18)				Rock (n = 10)				Dust (n = 54)			
	Unit	*Mean*	*Med*	*Min*	*Max*	*Mean*	*Med*	*Min*	*Max*	*Mean*	*Med*	*Min*	*Max*
Al	%	10.7	3.5	2.5	13.3	2.7	2.3	0.7	6.6	7.1	0.7	5.3	8.7
As	ppm	9.0	5.4	2.5	17.0	9.3	23.5	0.5	76.0	10.8	2.9	5.9	19.0
Ba	ppm	480.6	198.3	210.0	1067.0	152.0	169.1	29.0	420.0	708.7	93.1	542.3	931.0
Ca	%	0.6	0.3	0.1	1.1	0.1	0.0	0.0	0.2	1.1	0.4	0.6	3.4
Cd	ppm	0.2	0.1	0.1	0.5	0.1	0.0	0.0	0.1	1.6	2.3	0.2	10.4
Ce	ppm	85.9	31.7	27.3	155.0	32.5	25.7	12.1	81.1	76.8	10.8	62.4	102.7
Co	ppm	11.4	4.5	3.4	23.0	21.0	17.0	2.5	43.6	11.2	3.6	6.9	31.5
Cr	ppm	73.8	29.4	24.0	110.0	28.0	22.6	10.0	71.0	80.8	30.1	31.0	151.2
Cs	ppm	8.7	3.7	1.4	14.0	2.4	1.9	0.1	5.7	7.6	1.9	5.4	11.5
Cu	ppm	31.7	15.4	5.0	74.0	7.3	3.9	5.0	16.9	124.3	182.5	24.0	1290.0
Dy	ppm	5.5	1.7	1.6	8.3	2.8	2.4	0.5	5.6	4.7	0.8	3.4	7.4
Er	ppm	3.1	0.9	1.1	4.9	1.7	1.5	0.3	3.5	2.6	0.4	1.8	3.8
Eu	ppm	1.5	0.6	0.4	2.9	0.6	0.5	0.1	1.2	1.3	0.2	1.0	1.8
Fe	%	4.4	1.5	1.0	5.9	2.2	1.8	0.5	6.1	3.1	0.5	2.3	4.3
Ga	ppm	28.2	9.1	7.0	37.0	7.0	6.3	2.0	18.0	16.6	2.1	12.8	22.0
Gd	ppm	6.1	2.0	1.5	9.7	2.5	2.1	0.6	5.0	5.0	0.8	3.8	7.5
Hf	ppm	7.0	2.5	2.0	13.0	7.3	8.5	0.5	22.0	6.0	2.8	2.2	17.3
Ho	ppm	1.1	0.3	0.3	1.7	0.6	0.5	0.1	1.2	0.9	0.1	0.6	1.3
K	%	1.9	0.8	0.7	3.4	1.2	1.1	0.3	3.1	2.5	0.3	1.9	3.8
La	ppm	50.7	16.9	15.6	76.6	16.6	11.8	7.2	39.3	39.2	5.3	31.9	52.7
Li	ppm	53.7	19.6	5.0	84.0	7.6	3.7	4.0	14.0	49.8	10.9	36.0	73.0
Lu	ppm	0.5	0.1	0.2	0.7	0.2	0.2	0.0	0.6	0.4	0.1	0.3	0.7
Mg	%	1.2	0.5	0.2	2.0	0.2	0.2	0.0	0.5	1.2	0.2	0.8	1.7
Mn	ppm	322.2	178.3	62.0	782.0	90.4	42.6	41.0	170.0	511.0	187.5	228.7	996.0
Mo	ppm	1.8	1.0	1.0	4.0	1.3	0.8	0.6	3.3	2.0	5.5	0.0	40.4
Nb	ppm	14.8	5.2	5.0	23.0	5.1	5.2	1.0	15.0	13.5	2.7	3.0	20.0
Nd	ppm	42.4	14.8	11.5	66.6	17.8	14.1	4.8	36.2	23.1	9.6	11.9	41.1
Ni	ppm	32.6	14.6	2.5	55.0	9.7	8.9	2.5	28.0	34.4	59.0	11.0	411.0
P	%	0.0	0.0	0.0	0.1	0.0	0.0	0.0	0.0	0.4	0.2	0.1	0.8
Pb	ppm	23.0	5.8	9.0	34.0	10.1	5.1	5.0	18.0	72.0	36.2	26.4	223.0
Pr	ppm	11.7	4.1	3.3	18.6	4.8	3.7	1.4	9.6	8.6	1.3	6.8	11.5
Rb	ppm	112.8	46.3	43.0	194.0	43.3	47.6	7.2	125.0	113.5	12.2	80.9	140.3
Sb	ppm	0.9	0.4	0.2	1.6	0.3	0.3	0.1	1.1	1.8	0.9	0.7	5.8
Sc	ppm	14.0	5.1	2.5	20.0	4.3	3.9	1.0	11.0	9.5	1.6	7.0	13.0
Sm	ppm	7.6	2.6	2.0	11.8	3.1	2.5	0.8	6.4	6.0	0.9	4.6	8.1
Sn	ppm	2.7	1.0	0.5	4.0	1.0	0.7	0.4	2.0	33.7	29.4	2.2	167.2
Sr	ppm	116.1	51.8	50.0	297.0	45.7	24.4	16.5	84.0	202.1	25.7	160.4	289.7
Ta	ppm	1.1	0.5	0.3	1.7	0.6	0.5	0.1	1.4	1.1	0.3	0.2	1.9
Tb	ppm	0.9	0.3	0.2	1.3	0.3	0.3	0.1	0.9	0.8	0.1	0.6	1.1
Th	ppm	22.6	10.9	5.7	57.9	5.9	5.4	1.4	15.1	12.1	1.6	9.3	16.8
Ti	%	0.4	0.1	0.2	0.6	0.2	0.2	0.0	0.6	0.4	0.1	0.2	0.6
Tl	ppm	0.6	0.3	0.3	1.1	0.2	0.1	0.1	0.3	0.6	0.2	0.3	0.9
Tm	ppm	0.5	0.1	0.2	0.7	0.3	0.2	0.1	0.6	0.4	0.1	0.3	0.6
U	ppm	3.9	1.2	1.6	6.0	1.9	1.9	0.5	4.8	3.6	0.7	2.7	6.0
V	ppm	103.3	37.5	28.0	156.0	51.7	58.0	11.0	164.0	74.3	13.0	57.0	139.2
W	ppm	5.6	6.9	1.0	31.0	260.9	298.1	0.1	734.0	2.2	0.5	1.0	3.7
Y	ppm	29.1	9.9	8.7	52.3	10.5	11.6	2.4	31.1	26.2	5.1	17.9	43.7
Yb	ppm	3.1	0.9	1.2	4.4	1.3	1.5	0.3	3.9	2.6	0.5	1.7	4.1
Zn	ppm	82.1	28.8	15.0	132.0	16.8	10.0	8.0	40.0	461.0	282.8	161.0	1473.4
Zr	ppm	242.0	97.2	110.0	494.0	250.7	286.7	14.8	728.0	212.7	113.6	37.0	681.9

$(Si_{3.47}Al_{0.53})\ O_{10}(OH)]$, and all smectite-rich crystals appear to contain at least some illite-like interlayers based on relatively high amounts of K^+. Stoichiometrically, the minerals observed with SEM-EDS are best quantified as varied ratios of kaolinite, illite and smectite layer types within a given crystal, whether a weathered primary silicate mineral precursor, or neoformed clay occurring as isolated crystals or clumps of crystals in weathering rinds on silt-sized precursors (Fig. 8). The most smectite-like analysis is from sample C-3, $(K_{0.09}Ca_{0.11})(Al_{1.37}Fe_{0.37}Mg_{0.36})\ (Si_{3.73}Al_{0.27})\ O_{22}(OH)_2$. The origin of layer charge (in this example, −0.31 mol per 2:1 layer) is the tetrahedral sheet, classifying the smectite as beidellite.

The mineralogy and chemical composition of the clays in samples other than C-3 is quite consistent, with an average composition ($N = 25$) of $(K_{0.28}Ca_{0.05})(Al_{1.55}Fe_{0.37}Mg_{0.22})\ (Si_{3.49}Al_{0.51})O_{10}(OH)_2$, corresponding to interstratified kaolinite (15%) – illite (45%) – smectite (40%). This interstratified clay type occurs in weathered crystals of micas as well as in weathering rinds (Fig. 8). In contrast, the smectite-dominated clays of sample C-3 have an average composition ($N = 17$) of $(K_{0.12}Ca_{0.11})(Al_{1.37}Fe_{0.45}Mg_{0.31})\ (Si_{3.66}Al_{0.34})O_{10}(OH)_2$ corresponding to 80% smectite, 5% kaolinite and 15% illite-like layers (i.e. K^+ in interlayer, but no expansion with EG). This result is nearly identical to the unit formula for a 2:1 clay using the bulk chemical composition measured by XRF of $(K_{0.13}Ca_{0.10})(Al_{1.40}Fe_{0.41}Mg_{0.30})\ (Si_{3.63}Al_{0.37})O_{10}(OH)_2$. This observation supports the XRD-based interpretation that the clay in sample C-3 is almost entirely smectite.

4.5. Modeling clay mineralogy

Analysis with NEWMOD confirms that sample C-3 is smectite-dominated, consisting of 40% discrete smectite and 45% smectite-rich illite–smectite [R0 I(0.2)/S], and 5% each of R3 illite(0.9)-smectite, discrete illite and kaolinite (Fig. 9). In terms of layer types, C-3 contains 80% smectite layers, 15% illite layers and 5% kaolinite layers (Figs. 9 & 10). Sample C-13 has a similar composition (Fig. 10). The modeled pattern for C-1 (Fig. 9), another smectite-rich sample, suggests the presence of four stacking sequences, including two smectite-rich interstratified minerals that comprise 90% of the clay mineralogy – R0 kaolinite(0.5)-smectite [R0 K(0.5)-S] and illite(0.4)-smectite [R0 I(0.4)-

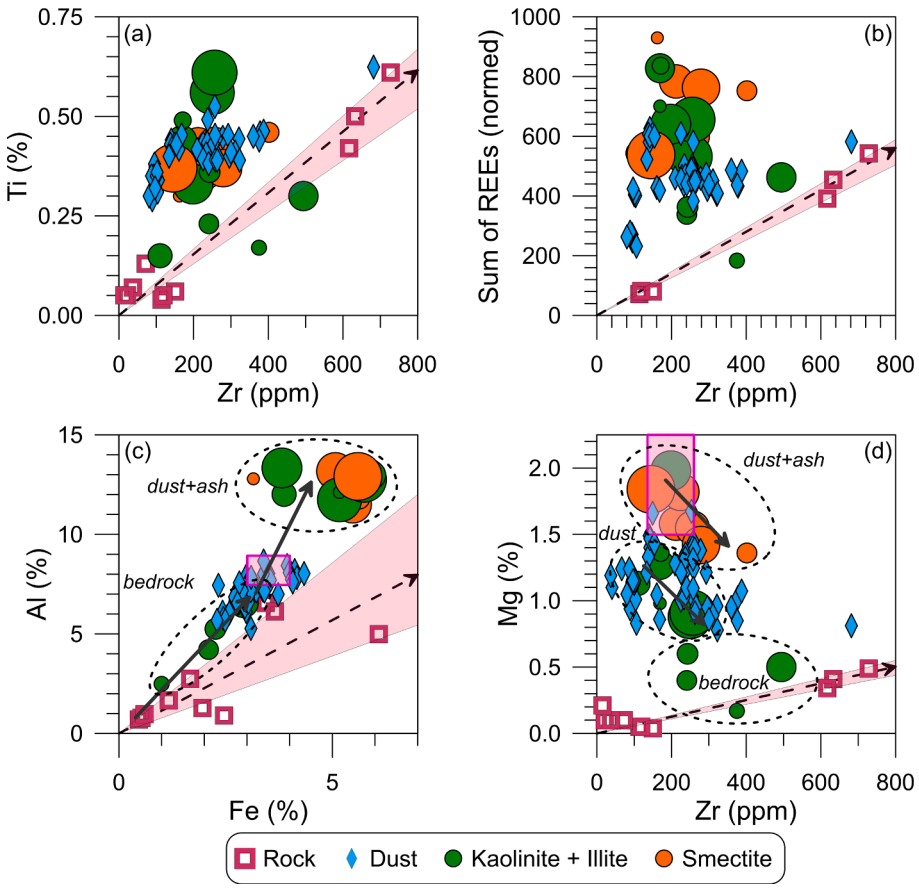

Fig. 5. (a-d) Scatterplots of immobile elements illustrating the similarity of dust and clay samples, and their divergence from local bedrock and the trend of increasing elemental abundance that would be expected from rock weathering (black dashed arrow with error envelope). Circle size for kaolinite + illite-dominated and smectite-dominated samples corresponds to total clay (<2 μm) content. Panels (c) and (d) also plot the compositional range (purple rectangle) reported for andesitic eruptive products from the Basin and Range province (Best et al., 1989). Dashed ovals surround groups of samples derived from parent materials dominated by local bedrock (primarily quartz with lesser illite and feldspars), dust (with more abundant feldspar, phengite and chlorite), and a combination of dust and ash (which has greater Mg due to the presence of biotite). Solid black arrows in panels (c) and (d) denote conceptual weathering trends. (For interpretation of the references to color in this figure legend, the reader is referred to the web version of this article.)

S] – plus ~ 5% each of discrete kaolinite and illite. In terms of layer types, C-1 consists of 50% smectite, 20% illite and 30% kaolinite layer types (Figs. 9 & 10). The mineralogy of samples C-2, C-4, C-6, C-11, C-15 and C-18 is similar to C-1 (Fig. 10), with varied ratios of the main phases observed, including discrete smectite, K-S (R0), I/S (R0, R1 or R3), and in some cases R0 K-I.

In contrast, XRD peaks in samples C-5, C-7 through C-12, C-14, C-16 and C-17 indicate an abundance of illite and kaolinite layer type relative to smectite (Fig. 10), with kaolinite and illite present as discrete crystals (or monomineralic layer sequences within crystals), as well as expandable interstratified phases. As exemplified by sample C-14 (Fig. 9), these clays exhibit an increase in intensity between 16 and 11 Å and reveal a weak peak at 19 Å when EG solvated, indicating an expandable 2:1 layer. Superimposed on the broad increase in intensity are small peaks at 14, 12 and 11 Å. The combined occurrence of the 19 Å (EG) peak and appearance of a weak 7.5 Å peak (EG) on the low angle side of the kaolinite 001 (7.17 A) indicates occurrence of kaolinite-smectite packets with 60–80% kaolinite layers (Moore and Reynolds, 1997), whereas peaks at 12 and 11 Å are produced by illite-rich I/S, R1 I(0.8)-S and R3 I (0.9)-S. Also in sample C-14 (Fig. 9), the low-angle shoulder on the 10 Å illite peak can be modeled with the 10.2 Å peak from R0 K(0.2)-I, i.e. interstratified illite-rich kaolinite-illite. In contrast, the 14 Å peak (EG) in C-14 is likely produced by hydroxyl-Al interlayers in a 2:1 mineral that prevents complete expansion to 17 Å with EG. This arrangement of a 2:1 layer with a hydroxyl-Al interlayer is termed hydroxy-interlayer smectite (or vermiculite) and is common in soils with at least moderate degrees of leaching (Meunier, 2007). Overall, the modelled C-14 consists of 35% discrete illite, 25% illite–smectite (R1 and R3), 20% kaolinite, 15% R0 kaolinite(0.6–0.8)-smectite, and 5% smectite (Fig. 9). This composition corresponds to 50% illite layers, 30% kaolinite layers and 20% smectite layers (Fig. 10).

5. Discussion

5.1. Clay mineralogy

The analyses reported here demonstrate that the clay minerals of the Uinta alpine zone represent varied interstratifications on a spectrum between smectite-rich (C-3, C-13) and illite + kaolinite-rich (e.g. C-12, C-14, C-16) (Fig. 10) as well as discrete zones or crystals where only one of these layer types is present for many layers consecutively. The range in abundance of kaolinite layers is 0 to 40%; illite layers range from 15 to 60% and smectite layers from 10 to 80%. On the basis of SEM-EDS analysis of clay crystals, the smectite in these soils is beidellite, similar in structure and composition to pedogenic clays reported from alpine (Egli et al., 2011, 2003), tropical (Ndayiragije and Delvaux, 2003; Ryan et al., 2016), and semi-arid (Ismail, 1970; Omdi et al., 2018; Righi et al., 1999a, 1999b; Van Ranst et al., 2020) environments. Overall, the transformation of biotite to beidellite is characterized by a decrease in interlayer K^+, tetrahedral Al, and octahedral Fe and Mg, accompanied by an increase in octahedral Al. Weathering of biotite to beidellite along this trajectory has been observed from semi-arid to humid climates (Ismail, 1970), as well as in acidic Spodosols (Egli et al., 2003; Gillot et al., 2000; McDaniel et al., 1995). In humid tropical environments, biotite may transform directly to kaolinite or halloysite (Ahn and Peacor, 1987), and although direct biotite-to-kaolinite conversion was not observed in this study, all micas examined by SEM-EDS appear to transform to interstratified clays containing kaolinite layer types.

5.2. Origin of the clay minerals

The combination of field observations, laboratory analyses and mineralogical modeling clearly establishes that the high elevation critical zone of the Uinta Mountains contains a diverse array of clay

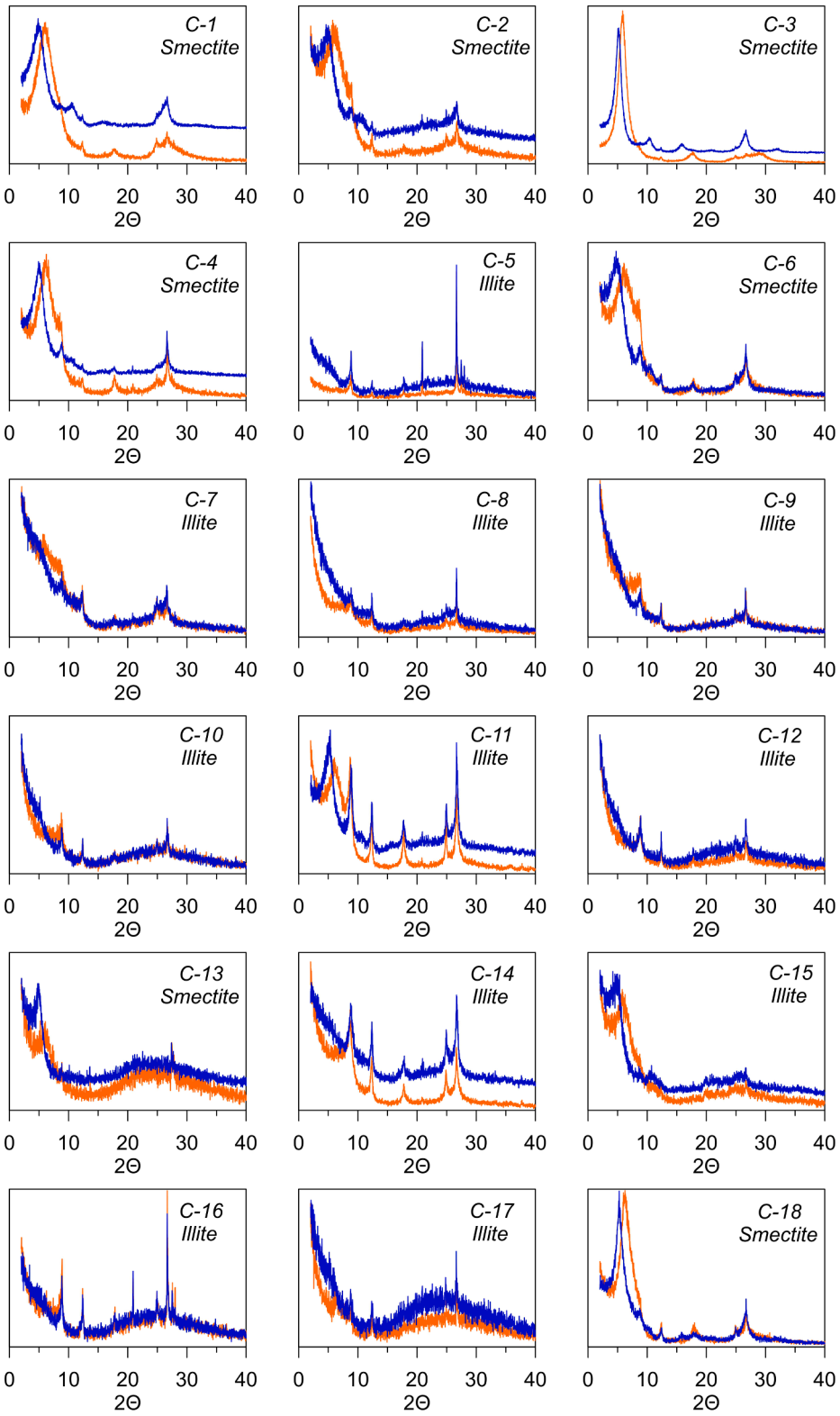

Fig. 6. XRD patterns for air-dried (orange) and ethylene glycol-treated (blue) clay fractions (<2 μm) of samples C-1 through C-18. Each sample is classified as either smectite-dominated or illite(kaolinite)-dominated. (For interpretation of the references to color in this figure legend, the reader is referred to the web version of this article.)

minerals in significant quantities despite a periglacial climate with underlying resistant siliciclastic bedrock. These clay-rich materials exhibit relatively bright orange hues and are highly weathered, with an average chemical index of alteration of 96.0 and low abundances of mobile Na and Ca. The geochemical signatures of immobile elements in these materials are similar to those in modern dust, and are notably different from the local bedrock (Fig. 5). This relationship strongly suggests that these clays have formed in situ through the weathering of primary minerals delivered through eolian activity. Furthermore, the relatively high amount of K^+ in the clay samples compared to Na^+ and Ca^{2+} is

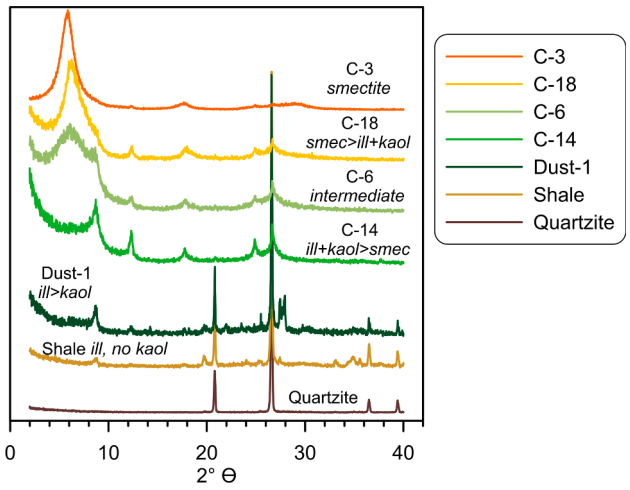

Fig. 7. XRD patterns for representative samples illustrating a progression from smectite-rich (C-3) to illite and kaolinite-rich interstratified K-I-S clay (C-14), with dust and local rock (shale and quartzite) samples presented for comparison. C-3, smectite-rich weathered tuff; C-18, smectite-rich interstratified K-I-S; C-6, intermediate K-I-S; C-14, interstratified K-I-S dominated by illite and kaolinite; modern dust from the Dust-1 sampler, illite > kaolinite with plagioclase and quartz; Shale bedrock, illite, but no kaolinite; Quartzite, no detectable minerals other than quartz. Note that the y-scale was stretched 3 × for the dust and rock samples to highlight peaks that would otherwise be obscured by the intensity of the main quartz peak.

consistent with K^+ retention in interlayers of 2:1 clays formed by weathering of mica and/or potassium feldspar, both of which are detectable in modern dust (Fig. 7) and are observed in SEM undergoing weathering to illite-rich interstratified K-I-S (Figs. 8 and 11).

On the other hand, in spite of the tendency of Mg^{2+} to be leached from soils, some samples have greater Mg content than modern dust. These relatively Mg-rich samples tend to be smectite-dominated (C-1, C-2, C-3, C-4, C-6, C-13, C-18) and are distinct from dust and illite + kaolinite-dominated interstratified clays on a plot of Zr vs. Mg (Fig. 5d). These smectite-rich samples plot in a field overlapping andesitic volcanic ashes from the Great Basin (Fig. 5d), which tend to contain 2.5–5.0% MgO (1.5 to 3.0% Mg) and 150–250 ppm Zr (Best et al., 1989). Thus, the smectite-dominated samples appear to be primarily derived from weathering of volcanic ash. Additional support for this interpretation comes from SEM-EDS analysis of the bentonite-like sample C-3, which revealed silt-to-sand sized clasts of volcanic glass and biotite weathering to Fe + Mg-bearing beidellite (Fig. 8).

Overall, absent an unidentified source of interstratified kaolinite-illite–smectite in the Uinta alpine zone, most of the expandable clays in these soils and regolith could not have formed through weathering of local bedrock. Instead, the majority of these clays formed through chemical weathering of micas (phengite, biotite, muscovite), volcanic glass, and feldspars delivered over the past 30 Ma in dust and volcanic ash, confirming the hypothesis of this study that clays in this alpine critical zone owe their origin to allochthonous minerals. Although it is possible that some of the clays observed in this system may have formed elsewhere and been transported to the Uinta Mountains by eolian processes, textures revealed in SEM analysis implies that the majority of these clays have formed in situ. By contrast, local bedrock appears to be the main source of parent materials for just 4 of the 18 samples (C-5, C-10, C-12, and C-17).

5.3. Pedogenic trajectories and paleoenvironmental considerations

Leaching over time will drive a soil system from parent material to smectite and eventually, if strong enough, towards kaolinite (Tardy and Roquin, 1992). In the case of the alpine critical zone of the Uintas, leaching operating on two different parent materials results in two different products of weathering: devitrified volcanic ash generates a smectite-dominated clay mineralogy, whereas weathering of eolian sediment rich in mica and feldspar produces assemblages dominated by interstratified illite and kaolinite layer types (Fig. 5d, 10). At the same time, minor contributions of weathered material from local bedrock, and mixing through cryoturbation and slope processes, produces additional clay mineral diversity.

Collectively, the available mineralogical and geochemical evidence illuminates six possible pathways from primary material to regolith or soil clays. Ash-rich (or pure ash) samples follow the pathways (1) Volcanic Glass → Ca-K Smectite (Beidellite), and (2) Biotite → Interstratified Kaolinite-Illite-Smectite (K-I-S). In original mixtures of ash and dust, (3) K-feldspar → Interstratified Illite-rich K-I-S. In relatively pure dust, (4) Phengite → Interstratified Illite-rich K-I-S. In mixtures of Dust + Local Bedrock (shale > quartzite), (5) Chlorite → Vermiculite. Finally, in some shale-rich parent materials, the weathering pathway is best described as (6) Illite → Interstratified Illite-rich K-I-S.

The chemical composition of beidellite formed by weathering of volcanic glass (as constrained by SEM-EDS) exhibits relatively low variability (Fig. 11), and its persistence – presumably for > 20 Ma – in this pedogenic environment, indicates that beidellite is a kinetically-favored, long-lived phase in this system. Direct weathering of volcanic glass to beidellite has been observed in field-based (e.g. McDaniel et al., 1995) and experimental (e.g. Kawano and Tomita, 1992) studies. The chemical transformation of biotite (Fig. 11), characterized by loss of Fe, Mg and K, and gain of Al and Ca, suggests that it also follows a trajectory towards beidellite-rich clay in these soils, and transformation of biotite to beidellite (as opposed to other layer types) is an expected transformation in semi-arid soil environments (Ismail, 1970). Furthermore, when biotite undergoes chemical weathering it may transform on a layer-by-layer basis to interstratified 1:1 and 2:1 layer types, with varied intensity of leaching at different microsites within the crystal causing different layer types to form (Aspandiar and Eggleton, 2006; Fordham, 1990; Hong et al., 2015). This process results in complex interstratifications of kaolinite, illite, vermiculite and smectite layer types, like those inferred for the samples analyzed in this study. At exposed edges, kaolinite is likely to form due to greater leaching, whereas 2:1 layers form where leaching is less intense, resulting in illite-like layers (where K^+ remains in the interlayer), smectite-like layers (where the interlayer is expandable), and vermiculite-like layers (where hydroxyl-Al interlayers occur).

The long-term stability of beidellite in soils like those of the Uinta alpine zone indicate that it may be useful as a paleoclimate indicator. The instability and high weathering rate of volcanic glass and biotite parent materials implies that the beidellites in these soils formed during early stages of pedogenesis (e.g. Egli et al., 2011, 2003; Pincus et al., 2017; Righi et al., 1999a), therefore chemical, isotopic or mineralogical signatures of beidellite may retain evidence of past soil conditions (e.g. Chamberlain and Poage, 2000). Beidellite is a common pedogenic mineral in a wide variety of environments, including: 1) temperate grasslands and beech forests of the South Island of New Zealand (Churchman, 1980); 2) some ustic climates (e.g. Thailand), where it is the dominant mineral in clay-rich Vertisols (Chittamart et al., 2010); 3) xeric climates (e.g. Sardinia, Sicily and southern Spain), where it occurs in thick clay-rich soils formed by weathering of Pleistocene to Miocene parent materials (Calero et al., 2013; Righi et al., 1998; Scalenghe et al., 2016); 4) coniferous forests where acidity in Spodosols causes high Al activity and formation of Al-beidellite (Egli et al., 2003; Gillot et al., 2000; McDaniel et al., 1995); and 5) lowland humid tropical systems where it persists as the main clay mineral for a short period (1 to 5 ka) before undergoing conversion to interstratified clay (mainly kaolinite-smectite) and then halloysite and kaolinite over 10 to 100 ka time scales (Pincus et al., 2017).

The chemical composition of pedogenic beidellite varies globally as a function of soil chemistry, and Uinta beidellites appear to reflect past

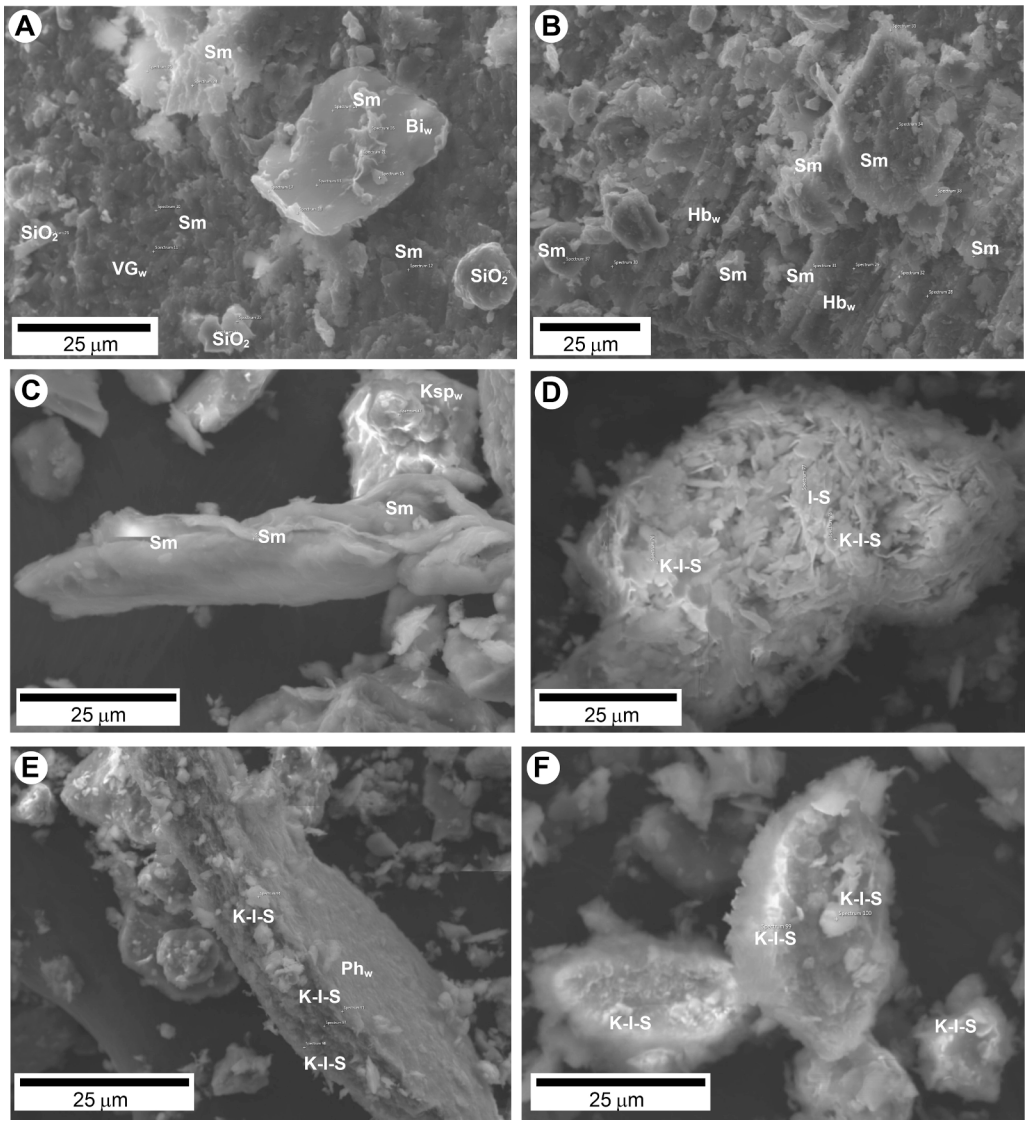

Fig. 8. SEM images showing the main textures and mineral types. Images A, B and C are from sample C-3 and show smectite-dominated (Sm) interstratified kaolinite-illite–smectite (K-I-S), which based on SEM-EDS compositions and XRD data contains 80% smectite layers. This pedogenic clay is forming by weathering of primary materials including biotite (Bi_w), an amorphous solid that is likely volcanic glass (VG_w), hornblende (Hb_w) and K-feldspar (Ksp_w). Images D, E and F (samples C-14, C-18 and C-18) are dominated by subequal amounts of kaolinite, illite and smectite layer types – as indicated by SEM-EDS and XRD – in varied stacking arrangements of K-I-S, regardless of primary solid parent material. Note precursor phengitic mica (Ph_m) in image E and textures indicative of weathering rinds on silt-sized clasts in D and F.

conditions more akin to monsoonal semi-arid, rather than acidic coniferous forest or humid tropical. Beidellite that forms in E horizons of Spodosols is Al-rich due to the high activity of Al in soil solutions of this soil order (Gillot et al., 2000; Righi et al., 1999b; Ross and Mortland, 1966). In contrast, the relatively Fe + Mg-rich octahedral sheets in Uinta soil beidellite (Fig. 11) are more similar to those that form in xeric (e.g. Badraoui and Bloom, 1990) or ustic (Chittamart et al., 2010) environments. At the same time, the illite + kaolinite-dominated interstratified clays with geochemical signatures similar to dust (Fig. 5) resemble interstratifed clays formed by weathering of micas, chlorite and feldspars in moderately leached soils ranging from mid-to-high elevation in the European Alps (Egli et al., 2003; Righi et al., 1999a), the semi-arid climate of Sardinia (Righi et al., 1999b) and monsoonal subtropical climate of south China (Hong et al., 2015). Formation of the smectite in Uinta alpine regolith and soils under seasonally moderate to high leaching intensity, perhaps associated with a monsoonal climate, is consistent with the available evidence.

5.4. Phases in the development of the Uinta alpine soil

Alpine soils in the Uinta Mountains are mixtures of parent material and weathering products integrated over the past ~ 30 Ma, initially dominated by ash from Oligocene volcanism (Best et al., 2013, 1989), and in more recent times, by eolian dust (Munroe et al., 2015) with a subordinate contribution from local bedrock. The general timeline of events and processes leading to the modern clay-rich regolith and soils of this environment can be divided into three phases.

Phase 1: Deposition of volcanic ash on the Gilbert Peak erosional surface beveled across the crest of the Uinta uplift (Bradley, 1936; Hansen, 1986) occurred during the Oligocene through the Miocene (~30 Ma to 15 Ma) as a result of volcanism in the Basin and Range province (Best et al., 2013, 1989). At the same time, climatic conditions ~ 5–6 °C warmer than modern prior to the mid-Miocene (Zachos et al., 2001) may have approached that of a monsoonal xeric climate, with seasonally high weathering rates that favored formation of beidellite from volcanic glass and biotite in this ash. Although deposition of eolian dust may have occurred simultaneously, ash was more abundant than dust as a parent material during this phase.

The stratigraphic record of Phase 1 is preserved as tuffs within the Bishop Conglomerate that caps the Gilbert Peak erosional surface, as well as in the younger Browns Park Formation (Hansen, 1986; Kowallis et al., 2005; Luft and Thoen, 1981; Powell and White, 1876; Sears, 1924). In the modern alpine zone, the tuffs of Phase 1 are represented by highly weathered deposits (e.g. sample C-3) that are locally present atop Uinta bedrock and below the ubiquitous layer of younger loess capping alpine soil profiles (Bockheim et al., 2000; Bockheim and Koerner, 1997;

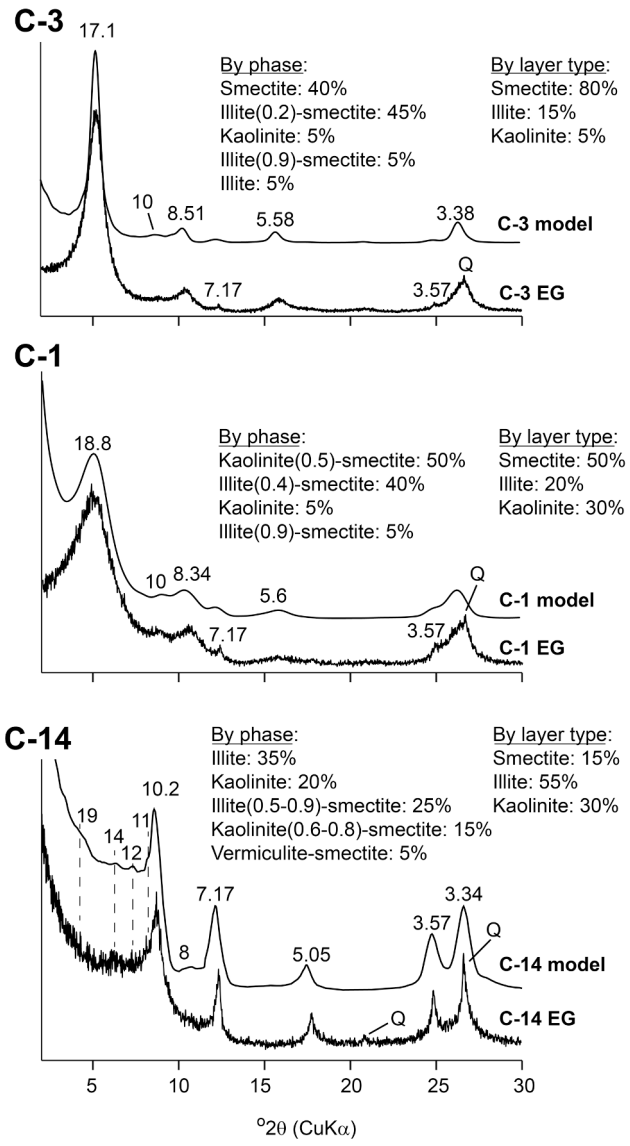

Fig. 9. Interpretation of clay mineralogy based on calculated patterns (top of each pair) compared to experimental patterns (bottom of each pair). Interstratified sequences (phases) are common (see text for terminology and details). Abundances of mineral types are shown by phase as well as by layer type.

Munroe, 2007). The Phase 1 landscape would have consisted of smectite-rich soils mantling a gently sloping eroded bedrock surface.

Phase 2: Ash deposition decreased as volcanism in the Basin and Range waned after ~ 18 Ma (Best et al., 2013). Simultaneously, dust became a more important soil parent material as climate transitioned towards the colder, drier Plio-Pleistocene (Zachos et al., 2001). Mica, chlorite and feldspar in this dust altered to illite + kaolinite-rich interstratified clay. Depending on rates of dust deposition and the amount of mixing, soils developed almost exclusively in dust may have come to overlie material derived from the weathering of older volcanic ash. These soil profiles likely exhibited alfic properties including the presence of argillic horizons.

Phase 3: Repeated climatic cycles, and persistently cold conditions (even during interglaciations), were the engine driving extensive cryoturbation and enhanced physical weathering during the Quaternary. This mixing effectively homogenized soil profiles, incorporating increasing amounts of material derived from the local bedrock (in both the fine and coarse fractions), and blurring distinctions between mineralogical end members originating from contrasting parent

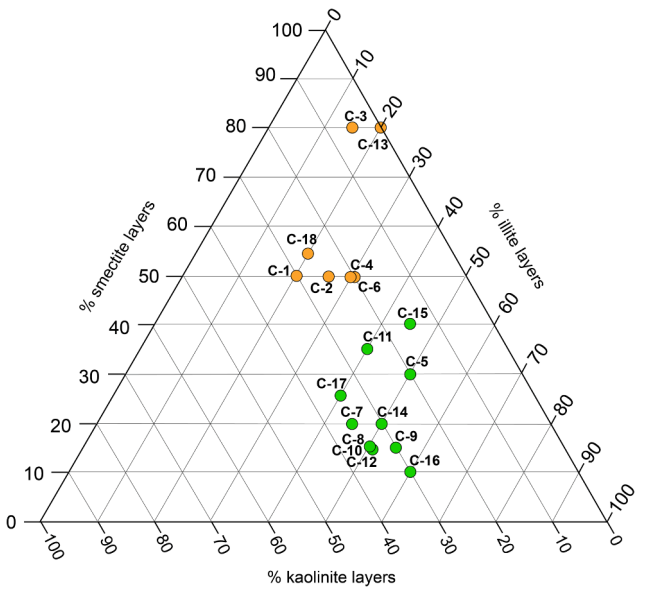

Fig. 10. Abundance of layer types in the < 2-μm fraction. All 1:1 aluminous clays are termed "kaolinite", all non-expandable 10 Å 2:1 layers are termed "illite", and all expandable 2:1 layers are termed "smectite". Orange circles are smectite-dominated and green circles are illite + kaolinite-dominated interstratified K-I-S clays. (For interpretation of the references to color in this figure legend, the reader is referred to the web version of this article.)

materials. During interglaciations, profile horizonation became distinct (as is the case today) as a cap of alpine loess accumulated at the top of the profile. However, accelerated cryoturbation during glacial episodes physically mixed dust into the solum, diminishing contrasts between surface and subsurface horizons (Munroe, 2007; Munroe et al., 2020). The classification of most Uinta alpine soils in the Inceptisol order of US Soil Taxonomy (Bockheim et al., 2000; Bockheim and Koerner, 1997; Munroe, 2007) reflects the tendency of cryoturbation to destroy horizonation, restricted plant growth in this environment, and intermixing of relatively unweathered siliciclastic material from the local bedrock.

An important corollary to this 3-phase history is that bedrock weathering has occurred at a slow rate relative to weathering of ash or dust in this critical zone over the past ~ 30 Ma. The low ratio of surface area to volume, and the lack of reactive minerals in this siliciclastic bedrock (relative to ash and dust), are the main factors influencing this slow weathering rate. Therefore, in comparison to other reports of pedogenic smectite in alpine environments (Egli et al., 2011, 2003, 2001b; e.g. Reynolds, 1971), the Uinta situation is one in which clays are present due to the weathering of allochthonous minerals rather than locally derived material. This insight underscores the crucial role of exogenous material, including dust (e.g. Aciego et al., 2017; Arvin et al., 2017), in the geoecological functioning of mountain ecosystems.

5.5. Limitations

Despite the success of this project in identifying the role of allochthonous minerals as a precursor for pedogenic clays in the Uinta alpine zone, the approach employed here has a few limitations that should be taken into consideration. The first of these relates to field sampling, which was restricted to just part of the extensive Uinta Mountain region. Although the 18 samples collected provide a good perspective on the properties of clay-rich soils and regolith in this study area, future work could focus on collecting additional samples from elsewhere in the Uinta Mountain alpine zone. Expansion to other settings would reveal whether other parts of the Uinta alpine zone, where potentially different facies of the diverse Uinta Mountain Group bedrock are present at the surface, exhibit contrasting clay mineralogies.

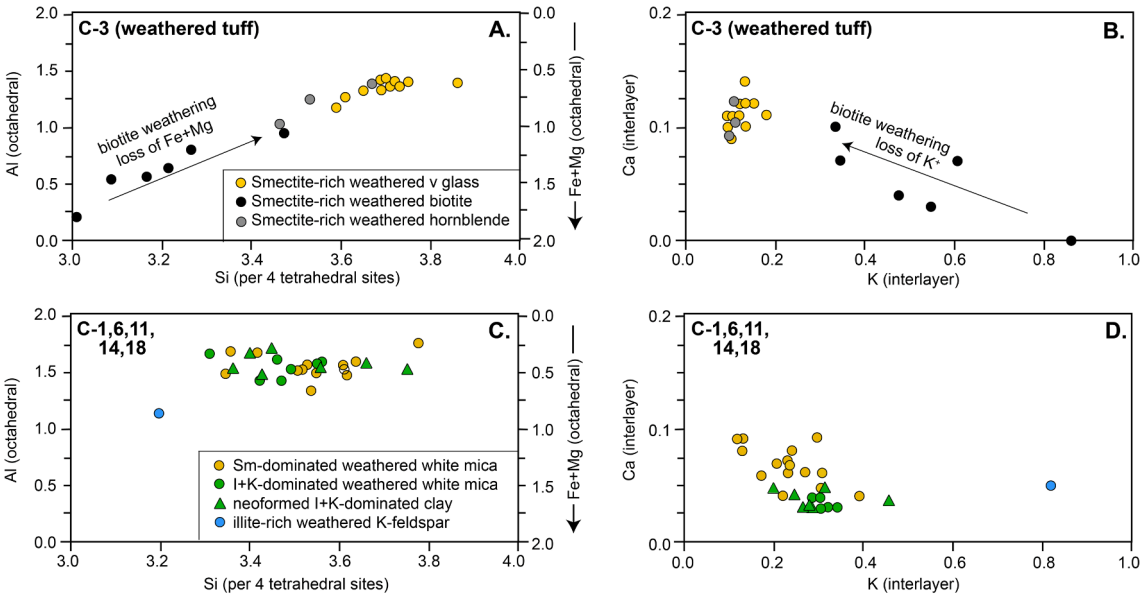

Fig. 11. SEM-EDS plots illustrating weathering trends and sample groupings. Note that octahedral Al is plotted on the left y-axis of panels A and C, and Fe + Mg is plotted on the right y-axis of panels A and C.

Second, the sampling strategy employed was by necessity opportunistic, taking advantage of natural exposures that could be safely accessed in the precarious location at the top of steep cirque headwalls (Fig. 2). Although there is no *a priori* reason to doubt that these exposures are reasonably representative, the fact is that the properties of the weathered material overlying the bedrock elsewhere in the Uinta alpine zone, but at depths greater than the ~ 100 cm that can be reached by hand excavation, remain poorly constrained. Furthermore, the three-dimensional extent of this body of weathered material is not well understood. Future work involving geophysics could be employed to ascertain the thickness and dimensions of this regolith in locations away from fortuitous natural exposures.

Finally, because the focus in this effort was on the clay fraction of the soil samples, bulk soil properties were not investigated. Inclusion of bulk soil analyses, evaluated in the context of prior work (e.g. Bockheim and Koerner, 1997; Munroe, 2007), could be an important aspect of future work in this mountain range.

6. Conclusion

The critical zone in alpine environments of the Uinta Mountains (Utah, USA) contains an abundance of clay minerals that is unexpected given a modern periglacial climate and resistant quartzite bedrock. Geochemical and mineralogical analysis reveals that samples of soil and regolith can be placed along a spectrum ranging from smectite-dominated, to those dominated by illite-rich interstratified kaolinite-illite–smectite (K-I-S). Ratios of immobile elements in most illite-rich samples are similar to those in modern dust, but are notably distinct from local bedrock. The origin of these clays is best explained by chemical weathering of mica and feldspar delivered by eolian processes over the past several million years. In contrast, smectite-dominated samples are distinct from both bedrock and local dust, particularly in terms of their higher Mg content. These samples apparently formed through the weathering of ash layers derived from volcanism in the Basin and Range province, which accumulated across the Uinta upland during the Oligocene. Devitrification of this ash and weathering of biotite led to the formation of smectite (specifically, beidellite enriched in Fe and Mg and with interlayer K^+ and Ca^{2+}) that is similar to the expandable clay reported from xeric to ustic conditions elsewhere in the world. Pervasive cryoturbation during the Quaternary has mixed these materials, often blurring distinctions between weathering products derived from originally contrasting parent materials. Although some of the sampled clay minerals may have been generated by weathering of local bedrock, the majority of the clay in these samples was produced through the weathering of allochthonous material (dust and ash). The capacity of these clays to retain K^+ and Ca^{2+} in interlayers is an important factor in soil fertility, and the long-term persistence of pedogenic beidellite may make it useful in analysis of paleoenvironment. The results of this investigation demonstrate that pedogenic clays can be common even in cold climates where soils and regolith occur atop resistant bedrock, emphasize that the clay inventory in surficial materials can reflect processes that operated before modern climatic conditions were established, and reinforce the key role played by exogenous mineral inputs in the alpine critical zone.

Declaration of Competing Interest

The authors declared that there is no conflict of interest.

Acknowledgments

Thanks to J. Bockheim, D. Douglass, and D. Koerner who played a key role in early research on Uinta alpine soils. L. Wasson provided significant assistance in the field, and J. Smith helped with the SEM analysis. We gratefully acknowledge insights from four anonymous reviewers.

Funding

This work was supported by US National Science Foundation award [EAR-1524476] to J. Munroe.

Data availability statement

Data generated in this project are available in the EarthChem repository at https://doi.org/10.26022/IEDA/111766.

References

Aciego, S.M., Riebe, C.S., Hart, S.C., Blakowski, M.A., Carey, C.J., Aarons, S.M., Dove, N. C., Botthoff, J.K., Sims, K.W.W., Aronson, E.L., 2017. Dust outpaces bedrock in nutrient supply to montane forest ecosystems. Nat. Commun. 8, 14800.

Ahn, J.H., Peacor, D.R., 1987. Kaolinitization of biotite; TEM data and implications for an alteration mechanism. Am. Mineral. 72, 353–356.
Alewell, C., Egli, M., Meusburger, K., 2015. An attempt to estimate tolerable soil erosion rates by matching soil formation with denudation in Alpine grasslands. J. Soils Sediments 15, 1383–1399. https://doi.org/10.1007/s11368-014-0920-6.
Allen, C.E., Darmody, R.G., Thorn, C.E., Dixon, J.C., Schlyter, P., 2001. Clay mineralogy, chemical weathering and landscape evolution in Arctic-Alpine Sweden. Geoderma 99, 277–294.
April, R., Newton, R., Coles, L.T., 1986. Chemical weathering in two Adirondack watersheds: Past and present-day rates. Geol. Soc. Am. Bull. 97, 1232–1238.
Arvin, L.J., Riebe, C.S., Aciego, S.M., Blakowski, M.A., 2017. Global patterns of dust and bedrock nutrient supply to montane ecosystems. Science. Advances 3, eaao1588.
Aspandiar, M., Eggleton, T., 2006. Weathering of biotite: micro to nano scale reactions in the regolith. Regolith. Citeseer 5–8.
Badraoui, M., Bloom, P.R., 1990. Iron-rich high-charge beidellite in Vertisols and Mollisols of the High Chaouia region of Morocco. Soil Sci. Soc. Am. J. 54, 267–274.
Best, M.G., Christiansen, E.H., Deino, A.L., Grommé, C.S., McKee, E.H., Noble, D.C., 1989. Eocene through Miocene volcanism in the Great Basin of the western United States. New Mexico Bureau Mines Mineral Resources Memoir 47, 91–133.
Best, M.G., Gromme, S., Deino, A.L., Christiansen, E.H., Hart, G.L., Tingey, D.G., 2013. The 36–18 Ma Central Nevada ignimbrite field and calderas, Great Basin, USA: multicyclic super-eruptions. Geosphere 9, 1562–1636.
Bockheim, J., Koerner, D., 1997. Pedogenesis in alpine ecosystems of the eastern Uinta Mountains, Utah. USA. Arct. Alp. Res. 29, 164–172.
Bockheim, J., Munroe, J., Douglass, D., Koerner, D., 2000. Soil development along an elevational gradient in the southeastern Uinta Mountains, Utah, USA. Catena 39, 169–185.
Bradl, H.B., 2004. Adsorption of heavy metal ions on soils and soils constituents. J. Colloid Interface Sci. 277, 1–18. https://doi.org/10.1016/j.jcis.2004.04.005.
Bradley, W.H., 1936. Geomorphology of the north flank of the Uinta Mountains. US Government Printing Office, Washington, DC.
Bryant, B., 2010. Geologic Map of the East Half of the Salt Lake City 1 x 2 Quadrangle (DuChesne and Kings Peak Quadrangles), Duchesne, Summit, and Wasatch Counties, Utah, and Uinta County. Utah Geological Survey Miscellaneous Publication, Wyoming.
Calero, J., Martín-García, J.M., Delgado, G., Aranda, V., Delgado, R., 2013. A nano-scale study in a soil chronosequence from southern Spain. Eur. J. Soil Sci. 64, 192–209.
Chamberlain, C.P., Poage, M.A., 2000. Reconstructing the paleotopography of mountain belts from the isotopic composition of authigenic minerals. Geology 28, 115–118.
Charbonnier, G., Duchamp-Alphonse, S., Deconinck, J.-F., Adatte, T., Spangenberg, J.E., Colin, C., Föllmi, K.B., 2020. A global palaeoclimatic reconstruction for the Valanginian based on clay mineralogical and geochemical data. Earth Sci. Rev. 202, 103092.
Chittamart, N., Suddhiprakarn, A., Kheoruenromne, I., Gilkes, R.J., 2010. Layer-charge characteristics of smectite in Thai vertisols. Clays Clay Miner. 58, 247–262.
Churchman, G.J., 1980. Clay minerals formed from micas and chlorites in some New Zealand soils. Clay Miner. 15, 59–76.
Darmody, R.G., Allen, C.E., Thorn, C.E., Dixon, J.C., 2001. The poisonous rocks of Kärkevagge. Geomorphology 41, 53–62.
Darmody, R.G., Thorn, C.E., Dixon, J.C., Schlyter, P., 2000. Soils and landscapes of Kärkevagge, Swedish Lapland. Soil Sci. Soc. Am. J. 64, 1455–1466.
Dehler, C.M., Porter, S.M., De Grey, L.D., Sprinkel, D.A., Brehm, A., 2007. The Neoproterozoic Uinta Mountain Group revisited; a synthesis of recent work on the Red Pine Shale and related undivided clastic strata, northeastern Utah, U. S. A. Special Publication - Society for Sedimentary Geology 86, 151–166.
Dixon, J.C., 1991. Alpine and subalpine soil properties as paleoenvironmental indicators. Phys. Geogr. 12, 370–384.
Dixon, J.C., Thorn, C.E., 2005. Chemical weathering and landscape development in mid-latitude alpine environments. Geomorphology 67, 127–145.
Dosseto, A., Buss, H.L., Suresh, P.O., 2012. Rapid regolith formation over volcanic bedrock and implications for landscape evolution. Earth Planet. Sci. Lett. 337, 47–55.
Egli, M., Dahms, D., Norton, K., 2014. Soil formation rates on silicate parent material in alpine environments: Different approaches–different results? Geoderma 213, 320–333.
Egli, M., Fitze, P., Mirabella, A., 2001a. Weathering and evolution of soils formed on granitic, glacial deposits: results from chronosequences of Swiss alpine environments. Catena 45, 19–47.
Egli, M., Mirabella, A., Fitze, P., 2003. Formation rates of smectites derived from two Holocene chronosequences in the Swiss Alps. Geoderma 117, 81–98.
Egli, M., Mirabella, A., Fitze, P., 2001b. Clay mineral formation in soils of two different chronosequences in the Swiss Alps. Geoderma 104, 145–175.
Egli, M., Mirabella, A., Mancabelli, A., Sartori, G., 2004. Weathering of soils in alpine areas as influenced by climate and parent material. Clays Clay Miner. 52, 287–303.
Egli, M., Wernli, M., Burga, C., Kneisel, C., Mavris, C., Valboa, G., Mirabella, A., Plötze, M., Haeberli, W., 2011. Fast but spatially scattered smectite-formation in the proglacial area Morteratsch: an evaluation using GIS. Geoderma 164, 11–21.
Fordham, A.W., 1990. Weathering of biotite into dioctahedral clay minerals. Clay Miner. 25, 51–63.
Freebairn, D.M., Loch, R.J., Silburn, D.M., 1996. Chapter 9 Soil erosion and soil conservation for vertisols. In: Ahmad, N., Mermut, A. (Eds.), Developments in Soil Science, Vertisols and Technologies for Their Management. Elsevier, pp. 303–362, 10.1016/S0166-2481(96)80011-0.
Gillot, F., Righi, D., Elsass, F., 2000. Pedogenic smectites in podzols from central Finland: an analytical electron microscopy study. Clays Clay Miner. 48, 655–664.
Goodfellow, B.W., 2012. A granulometry and secondary mineral fingerprint of chemical weathering in periglacial landscapes and its application to blockfield origins. Quat. Sci. Rev. 57, 121–135.
Grissinger, E., 1966. Resistance of Selected Clay Systems to Erosion by Water. Water Resour. Res. 2, 131–138.
Hall, K., 1995. Freeze-thaw weathering: the cold region "panacea". Polar Geogr. 19, 79–87.
Hall, K., Thorn, C.E., Matsuoka, N., Prick, A., 2002. Weathering in cold regions: some thoughts and perspectives. Prog. Phys. Geogr. 26, 577–603.
Hansen, W.R., 1986. Neogene tectonics and geomorphology of the eastern Uinta Mountains in Utah, Colorado, and Wyoming. United States Geological Survey, Professional Paper, p. 75.
Harnois, L., 1988. The CIW index: a new chemical index of weathering. Sed. Geol. 55, 319–322.
Hong, H., Cheng, F., Yin, K., Churchman, G.J., Wang, C., 2015. Three-component mixed-layer illite/smectite/kaolinite (I/S/K) minerals in hydromorphic soils, south China. Am. Mineral. 100, 1883–1891.
Ismail, F.T., 1970. Biotite weathering and clay formation in arid and humid regions, California. Soil Sci. 109, 257–261.
Kawano, M., Tomita, K., 1992. Formation of allophane and beidellite during hydrothermal alteration of volcanic glass below 200 C. Clays Clay Miner. 40, 666–674.
Kowallis, B.J., Christiansen, E.H., Balls, E., Heizler, M.T., Sprinkel, D.A., 2005. The Bishop Conglomerate ash beds, south flank of the Uinta Mountains, Utah: Are they pyroclastic fall beds from the Oligocene ignimbrites of western Utah and eastern Nevada? Uinta Mountain Geology. Utah Geological Association 131–145.
Luft, S.J., Thoen, W.L., 1981. Measured Sections of the Browns Park Formation (Miocene) in Moffat County, Colorado, 1980 (No. 81–171). US Geological Survey.
McDaniel, P.A., Falen, A.L., Tice, K.R., Graham, R.C., Fendorf, S.E., 1995. Beidellite in E horizons of northern Idaho Spodosols formed in volcanic ash. Clays Clay Miner. 43, 525–532.
Meunier, A., 2007. Soil hydroxy-interlayered minerals: a re-interpretation of their crystallochemical properties. Clays Clay Miner. 55, 380–388.
Moore, D.M., Reynolds, R.C., 1997. X-ray Diffraction and the Identification and Analysis of Clay Minerals. Oxford University Press, Oxford, England.
Muhs, D.R., Benedict, J.B., 2006. Eolian additions to late Quaternary alpine soils, Indian Peaks Wilderness Area, Colorado Front Range. Arct. Antarct. Alp. Res. 38, 120–130.
Munroe, J.S., 2014. Properties of modern dust accumulating in the Uinta Mountains, Utah, USA, and implications for the regional dust system of the Rocky Mountains. Earth Surf. Process. Landforms 39, 1979–1988.
Munroe, J.S., 2008. Alpine soils on Mount Mansfield, Vermont, USA: pedology, history, and intraregional comparison. Soil Sci. Soc. Am. J. 72, 524–533.
Munroe, J.S., 2007. Properties of alpine soils associated with well-developed sorted polygons in the Uinta Mountains, Utah. USA. Arct. Antarct. Alp. Res. 39, 578–591.
Munroe, J.S., 2006. Investigating the spatial distribution of summit flats in the Uinta Mountains of northeastern Utah, USA. Geomorphology 75, 437–449.
Munroe, J.S., Attwood, E.C., O'Keefe, S.S., Quackenbush, P.J., 2015. Eolian deposition in the alpine zone of the Uinta Mountains, Utah, USA. Catena 124, 119–129.
Munroe, J.S., Farrugia, G., Ryan, P.C., 2007. Parent material and chemical weathering in alpine soils on Mt. Mansfield, Vermont, USA. Catena 70, 39–48.
Munroe, J.S., Laabs, B.J.C., 2009. Glacial Geologic Map of the Uinta Mountains Area, Utah and Wyoming. Utah Geological Survey Miscellaneous Publication 09-4DM.
Munroe, J.S., Norris, E.D., Carling, G.T., Beard, B.L., Satkoski, A.M., Liu, L., 2019. Isotope fingerprinting reveals western North American sources of modern dust in the Uinta Mountains, Utah, USA. Aeolian Res. 38, 39–47.
Munroe, J.S., Norris, E.D., Olson, P.M., Ryan, P.C., Tappa, M.J., Beard, B.L., 2020. Quantifying the contribution of dust to alpine soils in the periglacial zone of the Uinta Mountains, Utah, USA. Geoderma 378, 114631.
National Research Council, 2001. Basic Research Opportunities in Earth Science. The National Academies Press, Washington, DC https://doi.org/10.17226/9981.
Ndayiragije, S., Delvaux, B., 2003. Coexistence of allophane, gibbsite, kaolinite and hydroxy-Al-interlayered 2: 1 clay minerals in a perudic Andosol. Geoderma 117, 203–214.
Norris, R.D., Jones, L.S., Corfield, R.M., Cartlidge, J.E., 1996. Skiing in the Eocene Uinta Mountains? Isotopic evidence in the Green River Formation for snow melt and large mountains. Geology 24, 403–406.
Olson, O.C., 1962. Some soil-plant-erosion relationships on the Leidy Peak Uinta alpine area. USDA Forest Service.
Omdi, F.E., Daoudi, L., Fagel, N., 2018. Origin and distribution of clay minerals of soils in semi-arid zones: Example of Ksob watershed (Western High Atlas, Morocco). Appl. Clay Sci. 163, 81–91.
Pincus, L.N., Ryan, P.C., Huertas, F.J., Alvarado, G.E., 2017. The influence of soil age and regional climate on clay mineralogy and cation exchange capacity of moist tropical soils: A case study from Late Quaternary chronosequences in Costa Rica. Geoderma 308, 130–148.
Powell, J.W., White, C.A., 1876. Report on the geology of the eastern portion of the Uinta Mountains and a region of country adjacent thereto.
Reynolds, R.C., 1971. Clay mineral formation in an alpine environment. Clays Clay Miner. 19, 361–374.
Reynolds, R.C., Hower, J., 1970. The nature of interlayering in mixed-layer illite-montmorillonites. Clays Clay Miner. 18, 25–36.
Righi, D., Huber, K., Keller, C., 1999a. Clay formation and podzol development from postglacial moraines in Switzerland. Clay Miner. 34, 319–332.
Righi, D., Terribile, F., Petit, S., 1999b. Pedogenic formation of kaolinite-smectite mixed layers in a soil toposequence developed from basaltic parent material in Sardinia (Italy). Clays Clay Miner. 47, 505–514.

Righi, D., Terribile, F., Petit, S., 1998. Pedogenic formation of high-charge beidellite in a Vertisol of Sardinia (Italy). Clays Clay Miner. 46, 167–177.
Ross, G.J., Mortland, M.M., 1966. A soil beidellite. Soil Sci. Soc. Am. J. 30, 337–343.
Ryan, P.C., Huertas, F.J., Hobbs, F.W.C., Pincus, L.N., 2016. Kaolinite and halloysite derived from sequential transformation of pedogenic smectite and kaolinite-smectite in a 120 ka tropical soil chronosequence. Clays Clay Miner. 64, 639–667.
Scalenghe, R., Territo, C., Petit, S., Terribile, F., Righi, D., 2016. The role of pedogenic overprinting in the obliteration of parent material in some polygenetic landscapes of Sicily (Italy). Geoderma 7, 49–58.
Sears, J., Graff, P., Holden, G., 1982. Tectonic evolution of lower Proterozoic rocks, Uinta Mountains, Utah and Colorado. Geol. Soc. Am. Bull. 93, 990–997.
Sears, J.D., 1924. Relations of the Browns Park Formation and the Bishop Conglomerate, and their role in the origin of Green and Yampa Rivers. Bulletin of the Geological Society of America 35, 279–304.
Singer, A., 1984. The paleoclimatic interpretation of clay minerals in sediments—a review. Earth Sci. Rev. 21, 251–293.
Singer, A., 1980. The paleoclimatic interpretation of clay minerals in soils and weathering profiles. Earth Sci. Rev. 15, 303–326.
Spinola, D.N., Pi-Puig, T., Solleiro-Rebolledo, E., Egli, M., Sudo, M., Sedov, S., Kühn, P., 2017. Origin of clay minerals in Early Eocene volcanic paleosols on King George Island, Maritime Antarctica. Sci. Rep. 7, 1–11.
Tardy, Y., Roquin, C., 1992. Geochemistry and evolution of lateritic landscapes Developments in Earth Surface Processes. Elsevier 407–443.
Thorn, C.E., Darmody, R.G., Dixon, J.C., Schlyter, P., 2002. Weathering rates of buried machine-polished rock disks, Kärkevagge, Swedish Lapland. Earth Surface Processes and Landforms: The Journal of the British Geomorphological Research Group 27, 831–845.
Thorn, C.E., Darmody, R.G., Dixon, J.C., Schlyter, P., 2001. The chemical weathering regime of Kärkevagge, arctic–alpine Sweden. Geomorphology 41, 37–52.
Thorn, C.E., Dixon, J.C., Darmody, R.G., Allen, C.E., 2006. A 10-year record of the weathering rates of surficial pebbles in Kärkevagge, Swedish Lapland. Catena 65, 272–278.
Thorn, C.E., Dixon, J.C., Darmody, R.G., Rissing, J.M., 1989. Weathering trends in fine debris beneath a snow patch, Niwot Ridge, Front Range, Colorado. Phys. Geogr. 10, 307–321.
Van Ranst, E., Kips, P., Mbogoni, J., Mees, F., Dumon, M., Delvaux, B., 2020. Halloysite-smectite mixed-layered clay in fluvio-volcanic soils at the southern foot of Mount Kilimanjaro. Tanzania. Geoderma 375, 114527.
Velde, B.B., Meunier, A., 2008. The origin of clay minerals in soils and weathered rocks. Springer, Berlin Heidelberg.
Wallace, C.A., 1972. A basin analysis of the upper Precambrian Uinta Mountain Group. Utah [Ph. D. thesis]: Santa Barbara, University of California 412.
Wedepohl, K.H., 1995. The composition of the continental crust. Geochim. Cosmochim. Acta 59, 1217–1232.
Zachos, J., Pagani, M., Sloan, L., Thomas, E., Billups, K., 2001. Trends, rhythms, and aberrations in global climate 65 Ma to present. Science 292, 686–693.